JGR Atmospheres

Key Points:

- Cloud properties are well-simulated compared to one satellite data set, and disagree more than they agree with ground-based instruments
- Eddy diffusivity-mass flux approach produces the deepest clouds and largest cell sizes
- Precipitation processes likely initiate cloud transition from closed to open cells

Simulating Mixed-Phase Open Cellular Clouds Observed During COMBLE: Evaluation of Parameterized Turbulence Closure

Timothy W. Juliano[1] [ID]**, Christian P. Lackner[2,3]** [ID]**, Bart Geerts[2]** [ID]**, Branko Kosović[1,4]** [ID]**,
Lulin Xue[1]** [ID]**, Peng Wu[5]** [ID]**, and Joseph B. Olson[6]** [ID]

[1]Research Applications Laboratory, U.S. National Science Foundation National Center for Atmospheric Research, Boulder, CO, USA, [2]Department of Atmospheric Science, University of Wyoming, Laramie, WY, USA, [3]Now at Brookhaven National Laboratory, Upton, NY, USA, [4]Now at Ralph O'Connor Sustainable Energy Institute, Johns Hopkins University, Baltimore, MD, USA, [5]Pacific Northwest National Laboratory, Richland, WA, USA, [6]NOAA/Global Systems Laboratory, Boulder, CO, USA

Abstract Marine cold-air outbreaks, or CAOs, are airmass transformations whereby relatively cold boundary layer (BL) air is transported over relatively warm water. To more deeply understand BL and mixed-phase cloud properties during CAO conditions, the Cold-Air Outbreaks in the Marine Boundary Layer Experiment (COMBLE) took place from late 2019 into early 2020. During COMBLE, the U.S. Department of Energy's first Atmospheric Radiation Measurement Mobile Facility (AMF1) was deployed to Andenes, Norway, far downstream (∼1,000 km) from the Arctic pack ice. This study examines the two most intense CAOs sampled at the AMF1 site. The observed BL structures are open cellular with high (∼3–5 km) and cold (−30 to −50 °C) cloud tops, and they often have pockets of high liquid water paths (LWPs; up to ∼1,000 g m^{-2}) associated with strong updrafts and enhanced turbulence. We use a high-resolution mesoscale model to explore how well four turbulence closure methods represent open cellular clouds. After applying a radar simulator to model outputs for direct evaluation, cloud top properties agree well with AMF1 observations (within ∼10%), but radar reflectivity and LWP agreement is more variable. Results suggest that the turbulent Prandtl number may play an important role for the simulated BL and cloud properties. All simulations produce enhanced precipitation rates that are well-correlated with a cloud transition. Finally, the eddy-diffusivity/mass-flux approach produces the deepest cloud layer and therefore the largest and most coherent cellular structures. We recommend the use of a non-local turbulence closure approach to better capture turbulent processes in intense CAOs.

Plain Language Summary Over the high latitude oceans, shallow clouds containing both liquid and frozen hydrometeors, or mixed-phase clouds, are frequently present. Moreover, they are important to the climate system due to their role in the radiation and moisture budgets. As a result of their microphysical makeup, they are especially challenging to simulate accurately for many numerical models across a range of spatial scales. To better understand these clouds during an intense outbreak of cold air from the Arctic, we utilize measurements from a recent field campaign called the Cold-Air Outbreaks in the Marine Boundary Layer Experiment (COMBLE). We complement the COMBLE observations with high-resolution numerical modeling to reveal more information about the cloud structures. We find that the simulated cloud properties, including morphology and abundance of liquid water at subfreezing temperatures, are dependent upon the method used to represent vertical turbulent exchanges between the ocean and atmosphere.

1. Introduction

The Arctic's atmospheric environment is complex, in part due to the presence of exposed land surface, sea ice, and open ocean that conspire to create a wide range of surface-atmosphere interactions. In this high-latitude region, where pack ice extends over much of the Greenland Sea during the cold season, synoptic-scale meteorological conditions often favor cold-air outbreaks (CAOs; e.g., Pithan et al., 2018). Widespread CAO conditions in the Arctic occur ∼25%–70% of the time during winter and spring in the Arctic and sub-Arctic (e.g., Fletcher et al., 2016; Mateling et al., 2023; Papritz & Spengler, 2017). One of the most intense air mass transformations on Earth occurs during these CAO conditions as cold Arctic air passes over the much warmer open ocean. Surface heat fluxes arising from air-sea interactions are amongst the highest observed on Earth (e.g., Papritz &

Spengler, 2017), supporting highly convective, mixed-phase clouds (MPCs) capable of producing intense precipitation, predominantly in the form of snow. These MPCs, which are an important component of the Arctic climate and Arctic amplification (e.g., Pithan et al., 2014), occur quite frequently. Based on a satellite climatology examining ice-free areas in the Norwegian and Barents Seas, Brümmer and Pohlmann (2000) conclude that organized convective patterns are present more than 50% of the time. Despite the profound impact that CAOs have on global atmospheric and oceanic circulations, surprisingly little is known about (a) their downstream evolution, (b) the relationship between their up- and downstream cloud morphologies, or (c) the connection between surface fluxes, boundary layer structure, cloud and precipitation properties, and mesoscale circulations.

Marine CAOs are rich in BL structure and convective cloud processes due to the tight coupling between the ocean and atmospheric BL in addition to complex motions spanning from the mesoscale to the microscale. Airmass lifetime over open water is important because mesoscale cloud organization and cloud properties evolve with fetch. Due to the interplay between strong wind shear and intense surface buoyancy, shallow, moist convection is initially organized into cloud streets ($0 < -z_i/L < 20$, where z_i and L are the BL depth and Obukhov Length) by a helical roll circulation that enhances surface fluxes (Renfrew & Moore, 1999). These roll clouds, which may extend for 100s of km, widen as the BL deepens (e.g., Young et al., 2002). Further downwind from the ice edge, the wind shear reduces (due to a weakening of the low-level ageostrophic wind component and turbulent mixing of momentum in the BL; Saggiorato et al., 2020), and the air-sea temperature contrast decreases. As the BL continues to grow, linearly aligned convection tends to transition to closed cellular convection, typically around $-z_i/L \approx 50$ (e.g., Khanna & Brasseur, 1998). The transition from closed to open cellular convection in marine CAOs tends to occur some distance further downstream (e.g., Wu & Ovchinnikov, 2022). Open cells tend to expand laterally before breaking up, with recent studies indicating the important roles of ice and precipitation processes (e.g., Eirund et al., 2019; Tornow et al., 2021).

These CAO cloud transitions, as vividly illustrated in satellite imagery, are believed to result from interactions between surface fluxes, BL circulations, turbulence, clouds, precipitation, and radiative processes. Numerical weather prediction (NWP) and climate models across a range of spatial scales continue to struggle with representing surface heterogeneities and related small-scale circulations (e.g., Bou-Zeid et al., 2020), which are critically important under CAO conditions. Intercomparison studies of marine CAO clouds using mesoscale models highlight the spread between models with respect to cloud organization (Tomassini et al., 2017) as well as phase partitioning and thus radiative fluxes (Field et al., 2017). Therefore, a better understanding of the complex interactions in CAO convection is especially pertinent for numerical models, as these interactions may be partially subgrid-scale and thus fall within a dynamic "gray zone" where mesoscale convective circulations and BL processes are tightly coupled and cannot be parameterized independently (Field et al., 2017). Furthermore, the resolution required to capture marine CAO convection in NWP models such as the Weather Research and Forecasting (WRF) model (Skamarock & Klemp, 2008; Skamarock et al., 2019) falls within the "Terra Incognita" (Wyngaard, 2004), where neither one-dimensional (1D) planetary boundary layer (PBL) parameterizations, nor subgrid turbulence parameterizations that are used in large-eddy simulation, are strictly applicable. The Terra Incognita broadly corresponds to horizontal grid cell spacings, $0.1 z_i < \Delta < z_i$ (Rai et al., 2019) where Δ is the horizontal mesh size.

Numerical modeling in the Terra Incognita or the gray zone of turbulence has been the focus of many recent studies in the field of BL meteorology (e.g., Angevine et al., 2020; Bogenschutz & Krueger, 2013; Ching et al., 2014; Efstathiou, 2023; Goger et al., 2019; Honnert et al., 2011; Ito et al., 2015; Juliano, Kosović, et al., 2022; Shin & Hong, 2015; X. Zhang et al., 2018; Zhou et al., 2014; Zonato et al., 2022). With respect to CAOs, de Roode et al. (2019) conducted a follow-up intercomparison study of the same CAO case examined by Tomassini et al. (2017) except using large-eddy simulation models. Within the Dutch Atmospheric Large-Eddy Simulation model (Heus et al., 2010), convergence in cloud properties across the range 0.25 km < Δ < 4 km was found at approximately $0.25 z_i$ (equivalent to $\Delta = 0.5$ km). Nonetheless, results were not consistent across participating models, motivating the need to utilize a single dynamical core that has multiple options to parameterize turbulence at mesoscale resolutions that fall within the turbulence gray zone.

In the present study, we use the WRF model to further explore how well some 1D turbulence closure methods can simulate the mesoscale organization and cloud microphysics and macrophysics of convective cells during two intense Arctic CAOs observed in March 2020. Sensitivity simulations focus on four turbulence closure approaches. The remainder of the paper is organized as follows. Section 2 outlines the measurements,

methodologies, and modeling configurations used to study the CAO cases. Analysis of the data, evaluation of the simulations, and examination of the airmass history are presented in Section 3. Lastly, a summary of our findings is provided in Section 4.

2. Data and Methods

2.1. The Cold-Air Outbreaks in the Marine Boundary Layer Experiment (COMBLE)

During the Arctic winter and spring of 2020, a U.S. Department of Energy (DOE)-funded field campaign called the Cold-Air Outbreaks in the Marine Boundary Layer Experiment (COMBLE; Geerts et al., 2022) deployed the DOE Atmospheric Radiation Measurement (ARM) Mobile Facility (AMF) #1 (Miller et al., 2016) at a coastal site in Andenes, Norway (70°N). This location collected data from 1 December 2019 to 31 May 2020, with a main goal to quantify properties of convective clouds that develop during Arctic CAOs. The campaign was largely successful: approximately 19% of campaign hours experienced CAO conditions at Andenes, Norway including several strong events (Lackner et al., 2023). While a wide range of CAO intensities were observed during COMBLE, here we focus on two of the strongest events—12–13 March and 28–29 March 2020 (hereafter referred to as 13 March and 28 March)—as recent works suggest that strong CAOs may occur more frequently under future climate scenarios (e.g., Dahlke et al., 2022).

Many measurements are available from AMF1 due to the large suite of instrumentation deployed during COMBLE. For this study, we rely on the sensitive narrow-beam 35 GHz Ka-Band ARM Zenith Radar (KAZR), which retrieves reflectivity, Doppler velocity, and Doppler spectral width. The direct KAZR measurements are available in the *ARSCLKAZR1KOLLIAS* data product on the ARM Data Archive (Clothiaux et al., 2001; Johnson & Jensen, 2019). We also utilize value-added products, including a multi-sensor product called *ARSCL-KAZRBND1KOLLIAS*, which contains cloud boundaries at a temporal resolution of 4 s and a vertical resolution of 30 m, based on KAZR, micropulse lidar, and ceilometer data (Johnson et al., 2019). The *INTER-POLATEDSONDE* product linearly interpolates available radiosonde data on a fixed time-height grid with a 1-min time resolution (Fairless et al., 2021). A liquid water path (LWP) product is provided by *MWRRET1LILJ-CLOU* based on microwave radiometer retrievals (Turner et al., 2007; D. Zhang, 2019). Following Crewell and Löhnert (2003) and Lackner et al. (2023), we remove LWP values below 30 g m^{-2} due to uncertainties related to the statistical retrieval method. All of these products are combined to better understand the open cellular cloud environment under CAO conditions as well as evaluate the WRF simulation performance.

2.2. Satellite Measurements

While the COMBLE observations provide a unique perspective into the CAO environment at the AMF1 site, a broader spatial perspective is desirable to better understand the convective cell structures, which spanned 10s of km during the two strong March cases. Therefore, we utilize polar-orbiting satellite retrievals from the Visible Infrared Imaging Radiometer Suite (VIIRS) onboard the Suomi National Polar-Orbiting Partnership (SNPP) and NOAA-20 spacecrafts. We use the Level-2 Cloud Properties files, which provide cloud information at a nominal resolution of 375 m, and we consider VIIRS measurements only when sufficient solar radiation is present (between ~8–13 UTC and ~7–14 UTC during the 13 and 28 March cases, respectively) to evaluate both directly retrieved and derived cloud variables. Upon inspection of the relative uncertainty of VIIRS-based cloud parameters of interest—namely, cloud top temperature and height, cloud water path, cloud optical thickness, and cloud effective radius—we choose to examine only cloud top temperature (CTT) because of its small relative uncertainty (typically less than 2% and weakly correlated with absolute CTT magnitudes; not shown). Under the MPC and high solar zenith angle conditions near Andenes during our events, the other variables show relative uncertainties ranging from approximately 10% to 50% and strong correlation with respective parameter magnitudes, thus making direct evaluation with WRF a challenge.

2.3. WRF Model

To simulate the 13 March and 28 March Arctic CAOs observed during COMBLE, we use version 4.4 of the WRF model (Skamarock & Klemp, 2008; Skamarock et al., 2019), which is the most widely used, community supported NWP framework. In the context of the two CAO cases examined here, we use the model to explore the mesoscale organization of convective cells near Andenes while highlighting the impacts of turbulence closure approaches on cloud properties.
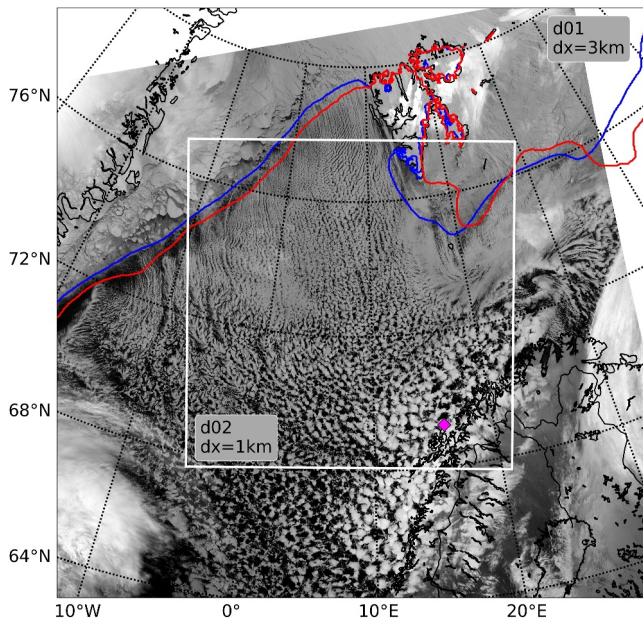
Figure 1. Infrared image of an example CAO cloud field from the 13 March 2020 case (~12 UTC retrieval from NOAA-20 VIIRS). The two-domain WRF configuration is also shown, with blue and red solid lines representing the pack ice edge (90% sea ice concentration) for the 13 March and 28 March cases, respectively. The location of Andenes, Norway is marked by the magenta diamond.

2.3.1. General Configuration

We set up a nested domain WRF simulation with $\Delta = 3$ km and $\Delta = 1$ km for the outer (d01) and inner (d02) domains, respectively (Figure 1). The number of grid cells in the x and y directions is 650×650 ($1,080 \times 1,080$) for d01 (d02), thus spanning a $1,950 \times 1,950$ km^2 ($1,080 \times 1,080$ km^2) region. We use a total of 136 vertical levels, with a vertical grid cell spacing of approximately 45 m from the surface to ~4.5 km AGL, and stretching above, to properly resolve the BL structure as the layer deepens from north to south. For each case, the simulations integrate for a total of 36 hr: the 13 March 2020 simulation begins at 12 UTC on 12 March and ends at 00 UTC on 14 March, while the 28 March 2020 simulation begins at 00 UTC on 28 March and ends at 12 UTC on 29 March. The first 12 hr are considered spin-up for the cloud field and thus not used in our study with the exception of the airmass history analysis for the 13 March case, which begins at 20 UTC on 12 March (see Section 3.6). We use the fifth generation ECMWF atmospheric reanalysis (ERA5; Hersbach et al., 2020) to provide the initial conditions and force the lateral boundary conditions every 3 hr. Sea ice concentration and sea surface temperature (SST) are also provided by ERA5 and updated every 3 hr.

2.3.2. Turbulence Closure Methods

We utilize two 1D PBL parameterizations in this study: Mellor-Yamada-Nakanishi-Niino (MYNN; Nakanishi & Niino, 2009) and Yonsei University (YSU; Hong et al., 2006). We now summarize and contrast these two turbulence closure methods, a necessary step to better interpret the findings presented in Section 3. In WRF, the MYNN scheme has three turbulence closure options: Level 2.5 and Level 3 eddy-diffusivity (ED) and Level 2.5 eddy-diffusivity/mass-flux (EDMF). The Level 2.5 ED approach is considered local, while the Level 3 ED and Level 2.5 EDMF approaches are considered non-local. Local schemes compute vertical turbulent mixing between only adjacent grid cells, while non-local schemes account for mixing within a deeper layer due to a superposition of eddies (e.g., Stull, 2012). Hereafter, we refer to the ED schemes as "Level 2.5" and "Level 3," and the EDMF scheme as "Level 2.5 EDMF" (Table 1).

The traditional Mellor-Yamada ED model is flexible such that turbulent fluxes and stresses may be represented using various levels of complexity (see, e.g., Mellor & Yamada, 1982); however, the Level 2.5 model is most often adopted due to its trade-off between reasonable accuracy and computational efficiency. In the Level 2.5 approach, turbulence kinetic energy (TKE) is computed prognostically, while potential temperature variance and the vertical turbulent stresses and scalar fluxes (in this example, potential temperature) are parameterized diagnostically. More specifically, a downgradient diffusion method is used to compute the zonal and meridional turbulent stresses and scalar fluxes

$$\langle u_j w \rangle = -K_{v,m} \frac{\partial U_j}{\partial z} \qquad (1)$$

Table 1
Various Turbulence Closure Configurations Considered for This Study

Reference name	Closure approach
Level 2.5	MYNN Level 2.5 ED (prognostic TKE, local)
Level 3	MYNN Level 3 ED (prognostic TKE and θ^2, non-local)
Level 2.5 EDMF	MYNN Level 2.5 ED (prognostic TKE, local) plus EDMF (non-local)
YSU	YSU (explicit entrainment mixing, non-local)

$$\langle w\theta \rangle = -K_{v,h}\frac{\partial \Theta}{\partial z} \tag{2}$$

where $j = 1,2$, U_j, and Θ are the mean momentum and potential temperature, $K_{v,m}$ is the vertical eddy viscosity, and $K_{v,h}$ is the vertical eddy diffusivity (used for heat, moisture, and other scalars). In local 1D PBL parameterizations that solve an equation for TKE, $K_{v,m}$ and $K_{v,h}$ usually take the general form

$$K_{v,m} = lqS_m \tag{3}$$

$$K_{v,h} = lqS_h \tag{4}$$

where l is a turbulent length scale, $q = \sqrt{2 \times TKE}$, and S_m and S_h represent stability functions for momentum and thermodynamics that depend upon buoyancy, vertical shear, and a set of closure constants.

The Level 3 model builds on the Level 2.5 model by computing the potential temperature variance prognostically. In this case, Equation 2 now becomes

$$\langle w\theta \rangle = -K_{v,h}\left(\frac{\partial \Theta}{\partial z} + \Gamma_\theta\right) \tag{5}$$

where Γ_θ is the so-called countergradient term, which enables the Level 3 model to represent countergradient flux through modification of S_h (Nakanishi & Niino, 2009). More practically, this means that the Level 3 model should be able to parameterize the (non-local) effect of large-scale eddies—which have horizontal length scales approximately equal to the BL depth under convective conditions—on vertical mixing of potential temperature, moisture, and condensate loads.

The main goal of the EDMF scheme is similar to that of the Level 3 model. However, the EDMF approach represents the countergradient flux differently, whereby it is assumed that a spectrum of buoyant plumes are responsible for the non-local (or countergradient) diffusion (Siebesma et al., 2007). This multiplume approach leads to the parameterization of turbulent scalar fluxes as

$$\langle w\theta \rangle = -K_{v,h}\frac{\partial \Theta}{\partial z} + \sum_{k=1}^{n} M_k(\Theta_{u_k} - \Theta) \tag{6}$$

where $k = 1, n$ represents an array of plume sizes (in MYNN, $n = 10$, such that a total of 10 plume sizes ranging from 100 to 1,000 m are represented), Θ and Θ_{u_k} represent the environmental and updraft potential temperature, and M_k is the convective mass flux represented as

$$M_k = A_{EDMF_k}(W_{EDMF_k} - w) \tag{7}$$

where A_{EDMF} is the grid cell fraction occupied by coherent convective updrafts (hence the non-local nature of this scheme), and w and W_{EDMF} represent the environmental and updraft velocities, respectively. In the MYNN EDMF scheme, A_{EDMF} is a function of the surface buoyancy flux, with an upper limit (=0.1) reached only for strong surface buoyancy fluxes (>250 W m^{-2}). The maximum value of A_{EDMF} is similar to other EDMF implementations that have set A_{EDMF} to a constant ranging from 0.04 to 0.1 (e.g., Köhler et al., 2013; Neggers et al., 2009; Soares et al., 2004; Suselj et al., 2014; Witek et al., 2011). Moreover, MYNN EDMF assumes that $w = 0$. More details regarding the MYNN-EDMF implementation are provided by Olson et al. (2019).

We note that the MYNN Level 2.5 closure has been tuned to be run with the mass-flux (MF) component and not the ED component in isolation. The ED has been greatly reduced in recent versions of WRF (since WRF v4.0) compared to the original implementation, when it was meant to be run in isolation. Thus, by itself, the ED is meant to handle only the stable boundary layer. As a result, our experimental design allows us to show the essential contribution of the non-local mixing by the MF scheme and the consequences of running without it when comparing the Level 2.5 and Level 2.5 EDMF results.

The YSU parameterization is a non-local closure scheme that is not TKE-based and thus computes $K_{v,m}$ differently than MYNN, viz.

$$K_{v,m} = k w_s z \left(1 - \frac{z}{z_i}\right)^p \tag{8}$$

where p is the profile shape exponent ($=2$), k is von Karman's constant ($=0.4$), w_s is the mixed-layer velocity scale, and z is the height above the surface. The BL height is defined as the level where the buoyancy flux, which is a function of virtual potential temperature (θ_v) and the bulk Richardson number, is a minimum. The $K_{v,h}$ term is then computed from $K_{v,m}$ through a Prandtl number relationship following Noh et al. (2003) (see Equation A4 in Hong et al. (2006)).

The turbulent fluxes are computed in a similar manner as in the Level 3 MYNN scheme; however, there is also consideration of the flux at the inversion layer through extension of the concept originally outlined in Hong and Pan (1996). This extension leads to an explicit treatment of entrainment following Noh et al. (2003). The general formula of the stress and scalar fluxes is

$$\langle w\phi \rangle = -K_{v,\phi}\left(\frac{\partial \Phi}{\partial z} - \gamma_\phi\right) - \langle w\phi \rangle_h \left(\frac{z}{h}\right)^3 \tag{9}$$

where ϕ is a prognostic variable, Φ is a mean state variable, $K_{v,\phi}$ is either $K_{v,m}$ or $K_{v,h}$ depending upon the variable of interest, γ_ϕ is a correction to the local gradient (akin to Γ_θ for the Level 3 MYNN scheme), and $\langle w\phi \rangle_h$ is the flux at the inversion layer.

It is clear that the various turbulence closure approaches compute the vertical stresses and fluxes (and therefore their divergences, which control the tendencies of the state variables) in fundamentally different ways. As momentum, heat, moisture, and condensate loads will be mixed in the vertical differently between the schemes, we expect that this will greatly impact CAO convective cell properties (e.g., liquid/ice partitioning) as well as mesoscale organization (e.g., cell size). We conduct four different simulations, each with a different turbulence closure option following our discussion in this section. The various configurations are outlined in Table 1.

2.3.3. Other Model Options

Our choice of additional model physics for the WRF simulations is as follows. Horizontal eddy diffusion is computed using the 2D Smagorinsky approach (coefficient set to 0.25; Smagorinsky, 1963), which is common practice for mesoscale simulations. While the horizontal eddy diffusion approach can affect the organization of convective structures (e.g., de Roode et al., 2022; Juliano, Kosović, et al., 2022; Simon & Chow, 2021), exploring this topic is beyond the scope of the present study. We activate the revised MM5 surface layer physics parameterization (Jiménez et al., 2012) and use the Noah-MP land surface model (Niu et al., 2011; Yang et al., 2011). Radiative transfer processes are treated using the Rapid Radiative Transfer Model for GCMs (RRTMG) shortwave and longwave schemes (Iacono et al., 2008).

An important physics choice for the case study here is the microphysics parameterization; we choose to use the Thompson-Eidhammer Aerosol-Aware microphysics scheme (Thompson & Eidhammer, 2014). A major advantage of this scheme is a prognostic treatment of so-called water- and ice-friendly aerosols. Recent developments to the WRF model described by Juliano, Jiménez, et al. (2022) allow us to use time-varying aerosol information from the GEOS-5 model. In the Thompson-Eidhammer microphysics parameterization, the water- and ice-friendly aerosols may act as nucleation sites (i.e., cloud condensation nuclei (CCN) and ice nucleating particles, respectively), therefore making the scheme double-moment (prediction of mass mixing ratio and number concentration) for cloud liquid water and rain water, in addition to cloud ice. The remaining water phase classes (i.e., snow and graupel) are treated as single-moment (prediction of only mass mixing ratio and assuming a particle size distribution). The microphysical tendencies of the mass mixing ratio and number concentration variables are handled by the microphysics scheme. The physical processes accounted for by the parameterization are described in Thompson et al. (2004, 2008) and Thompson and Eidhammer (2014).

2.4. Comparing Observations and Model

Critical to the success of this study is a meaningful evaluation of the WRF model using both the AMF1 COMBLE measurements and the satellite retrievals. To ensure a fair model evaluation, we apply the Cloud-resolving model Radar SIMulator (CR-SIM; Oue et al., 2020) to the WRF outputs before comparison with the COMBLE observations. First, we produce 2D (time-height) model outputs at high temporal frequency (i.e., the native model time step of 3 s for d02) at the AMF1 location using virtual towers through WRF's *tslist* option. Then, we provide CR-SIM with the necessary information with respect to the KAZR specifications and run the forward simulator on the 2D WRF outputs to produce time-height radar-equivalent moments. Cloud top height and temperature from the model outputs are determined using a range-dependent dBZ threshold as defined by CR-SIM.

For the comparison between WRF and the satellite retrievals, we collect all available NOAA-20 VIIRS and SNPP VIIRS scenes during our simulation periods. For the 13 March (28 March) case, we consider a total of 5 and 6 scenes (4 and 6) from NOAA-20 and SNPP, respectively. Given our model output frequency of 30 min, there is a maximum of 15 min time offset between the simulations and observations. To estimate the modeled CTT, we follow the approach of Huang et al. (2014) to identify cloud top using a 0.1 cloud optical thickness threshold. Under this approach, it is assumed that the CTT retrieved by the VIIRS instrument is in response to the bulk emissivity of the hydrometeors at some optical depth into the cloud. We compute cloud optical thickness by integrating downward beginning at the top of the model domain while using constant absorption coefficients of 0.145, 0.00033, 0.0735, and 0.00234 m^2 g^{-1} for cloud liquid water, rain water, cloud ice, and snow, respectively, following Dudhia (1989).

3. Results

3.1. Large-Scale Meteorology

We begin our analysis by examining the synoptic scale patterns at 925 and 500 hPa for the 13 March and 28 March CAO cases at 12 UTC (Figure S1 in Supporting Information S1). These times are selected to approximately represent the middle of the intense CAO conditions. A key feature defining a CAO is evident in both cases, evidenced by a broad region of cold air advection that spans from over the pack ice to over the much warmer open ocean. The marine CAO (MCAO) index, which is defined as $\theta_{SST} - \theta_{850hPa}$, is hatched where MCAO ≥ 8 K to indicate intense convective conditions driven by the strong air-sea thermal contrast. For both events, MCAO ≥ 8 K are found over much of the open ocean, including at and just upstream of the AMF1 site, suggesting that it is a meaningful region to explore convective cell properties. In the 13 March case, the strong equatorward winds at 925 hPa are directed more northerly than in the 28 March case due to the orientation of the geopotential height contours. Meanwhile, at 500 hPa, the winds are relatively weak and the air is very cold (following a closed low or trough) over the CAO region in both cases, with stronger winds toward the west associated with an advancing warm front. The very cold air at 500 hPa is consistent with a lack of capping of surface-driven convection in both cases (not shown). In general, the background large-scale forcing is similar in both cases.

3.2. Mesoscale Cell Organization

In the northern portion of our WRF domains, where convective roll structures are observed by satellite imagery, our simulations cannot properly resolve the features (and, in fact, instead produce spurious structures; e.g., Ching et al., 2014; Zhou et al., 2014) because Δ is much too large relative to z_i (~1,000 m). In fact, findings from Lai et al. (2020) suggest that $\Delta \approx 100$ m is required to resolve convective roll structures in the Arctic. Therefore, given that the numerical model's Δ should be much less than z_i in order to properly resolve turbulent features (Rai et al., 2019), in this study, we focus on the large convective cells downstream near Andenes that are well resolved by the inner domain (d02).

We begin by asking the question: how do the different PBL schemes capture this open cellular convection? Figure 2 shows a snapshot in time (12 UTC) from the 13 March 2020 case: vertical velocity field at $0.5z_i$, horizontal divergence at 100 m AGL, and 2-m temperature. Together, these three fields reveal cell structure, size, and intensity. While each of the four model configurations develops organized cellular structures, they each resolve cells with different characteristics. First, the structures appear to be least organized in the Level 3 simulation, evidenced by disconnected updrafts. In the Level 2.5 and YSU simulations, the structures are slightly more organized, with more coherent updrafts. The most organized cellular structures are seen in the Level 2.5
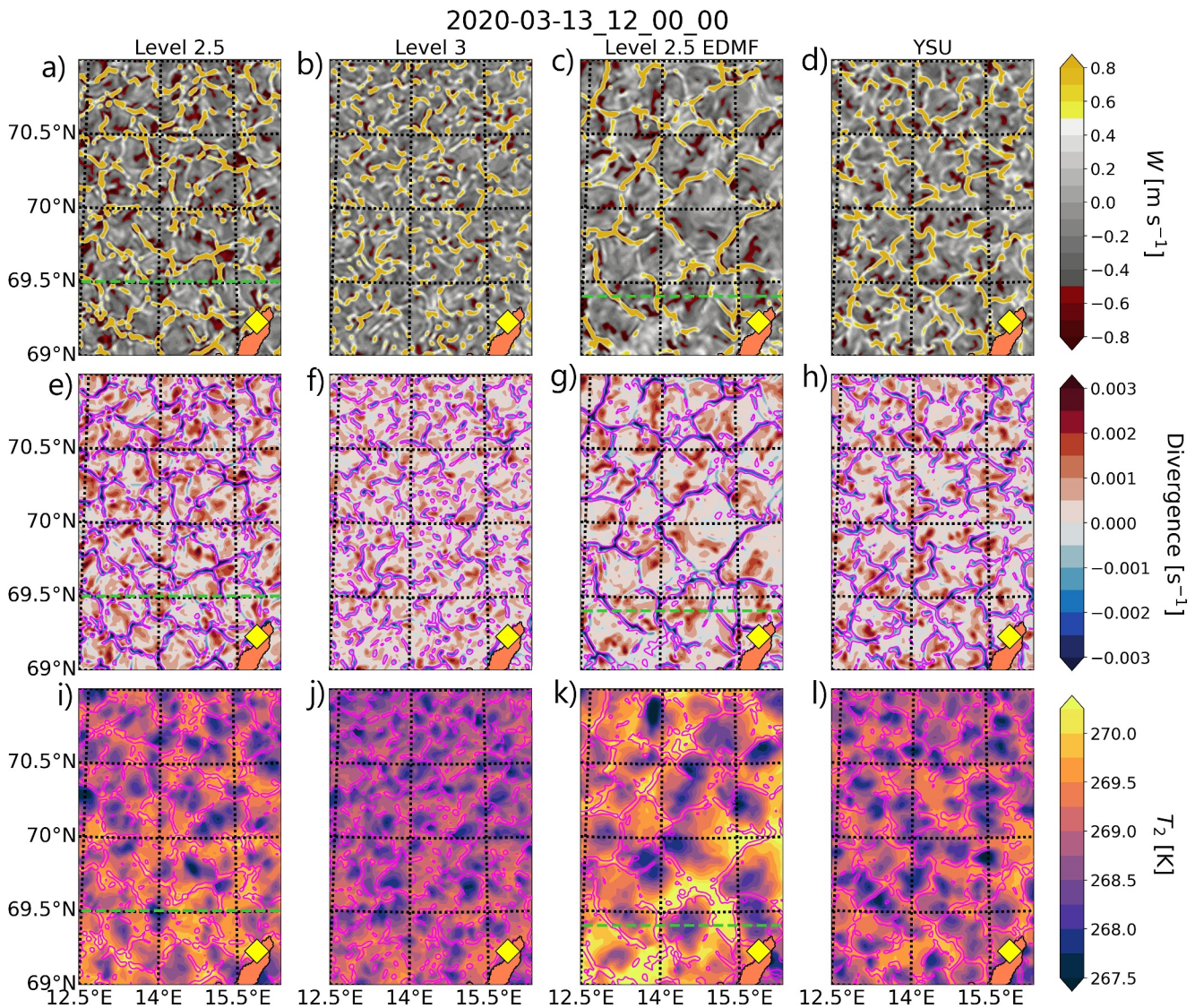
Figure 2. Snapshots at 12 UTC on 13 March of convective cell properties near AMF1 at Andenes, Norway for the four WRF configurations: (a–d) vertical velocity (W) at $0.5z_i$, (e–h) divergence at 100 m AGL, and (i–l) 2 m temperature with $W > 0.25$ m s^{-1} at $0.5z_i$ shown in magenta contours for reference. Fields are contoured according to their respective colorbars. The location of the AMF1 is marked by the yellow diamond. The locations of the vertical cross sections shown in Figures 8 and 9 are represented by the dashed green lines for the Level 2.5 and Level 2.5 EDMF results.

EDMF simulation. Accordingly, the sizes of the cells follow a similar trend, with the Level 2.5 EDMF configuration clearly simulates the largest structures. To support this statement, a quantitative analysis of the cell sizes will be presented later.

The near-surface horizontal divergence field aligns well with the resolved vertical motions in the middle of the BL: updrafts (downdrafts) correlate with regions of convergence (divergence). Examining the 2-m temperature field suggests that cold pools are closely associated with mid-BL downdrafts and low-level divergence. These cold pools, which have received much attention in the literature, are likely generated due to falling precipitation and related evaporation and/or sublimation (e.g., Saggiorato et al., 2020; Seifert & Heus, 2013; Torri et al., 2015). We will further investigate the cell vertical structure in Section 3.5.

While Figure 2 provides a visual depiction of the cellular structure during the strong CAO of 13 March, it is merely qualitative. To determine the characteristic cell sizes quantitatively, we follow work by Haerter et al. (2017) and Eirund et al. (2019) and apply a two-point correlation method to the horizontal divergence field. The characteristic cell size of a particular scene (termed the "organization scale" by Haerter et al. (2017)) is then

determined from the minimum correlation. We consider the southernmost ∼75% of the domain shown in Figure 2 to compute the correlation function at 30 min intervals (i.e., the output frequency of our WRF simulation) on a square domain for the duration of the two CAO events after model spin-up. More details of the approach, including its inherent limitations, are contained in Text S1 of the Supporting Information S1.

In Figure 3a, we show an example of the normalized correlation coefficient for the same time as in Figure 2. At any given time when the 2D divergence field is analyzed, the correlation function yields a clear first local minimum, which is indicative of the cell center and thus a quantitative measure of the organized cell size (Haerter et al., 2017). As visually shown in Figure 2, for this particular time, the Level 3 model produces the smallest cells, followed by the Level 2.5 and YSU models, and finally the Level 2.5 EDMF scheme simulating the largest cells.

The cell sizes computed for the entirety of the 13 March and 28 March events are plotted in Figures 3b and 3c. In both cases, the mean cell sizes are lowest for the Level 2.5 and Level 3 configurations, which both show values of ∼12–14 km. For both of these PBL schemes, the values are often small (∼10 km). In the case of the Level 3 scheme, we suspect this may be due to ill-defined cell structures, which likely are not suitable for the correlation method. For the Level 2.5 scheme, the reason may be more complicated (see Text S1 in Supporting Information S1). Meanwhile, the YSU and Level 2.5 EDMF schemes yield substantially larger cells of ∼23–25 km and ∼33–38 km in size, respectively. The values shown by YSU, and to a lesser extent Level 2.5 EDMF, appear more reasonable than those shown by Level 2.5 and Level 3, as a recent study by Wu and Ovchinnikov (2022) used MODIS imagery to estimate mean cloud major axis lengths of ∼20–25 km for this region during both CAO events (see their Figure 6). Nonetheless, the Level 2.5 EDMF scheme sometimes produces very large cell sizes (>50 km), which are likely unreasonable. We note that while the two-point correlation method considers all the structures from a single snapshot in time, the correlations for a given distance are averaged together. Thus, Figure 3 does not highlight the potential distribution of cell sizes, which may be broader for one PBL scheme than another.

The cell sizes simulated by the YSU and Level 2.5 EDMF scheme can be contrasted with the model's effective resolution of ∼6–7Δ (Skamarock, 2004), or 6–7 km for d02. Given that this is much less than the observed cell sizes, we can confidently state that our WRF simulation can resolve the convective structures near Andenes. Even still, the PBL schemes considered here are 1D and thus are not able to properly account for horizontal gradients, which likely are non-negligible when simulating the narrow updrafts prevalent in this environment.

3.3. Top-Down Perspective From Satellite

We now begin to connect the mesoscale organization to cloud properties by comparing the satellite retrievals of CTT to those estimated from the WRF output. In Figure S2 of the Supporting Information S1, we show a snapshot of the CTT field from the 13 March case retrieved by the NOAA-20 VIIRS satellite as well as simulated from the four WRF configurations. Similar to our findings with respect to cell size, the cloud features—represented by organized structures in the CTT field—are largest in the Level 2.5 EDMF scheme. The cells from the Level 2.5 and YSU simulations are notably smaller, and the Level 3 model even still smaller. Furthermore, the relatively abundant cold CTT regions observed by VIIRS appear to be best represented by the Level 2.5 EDMF scheme.

Upon compiling numerous VIIRS retrievals from the 13 and 28 March CAO cases, we more robustly compare the WRF simulations to the satellite CTT measurements (Figure 4). For the 13 March (28 March) case, the VIIRS retrievals show median CTT values of approximately −40°C (−36°C), respectively. The satellite distributions have a dominant mode around these median values for both cases. While the 13 March case shows only this single mode, the 28 March case displayed a secondary broad mode near −28°C to −20°C. The warmer CTT mode may be related to cloud edges that are characterized by relatively shallow tops. All four WRF simulations capture the relatively colder CTTs in the 13 March case compared to the 28 March case. According to the satellite measurements during the two events, the Level 2.5 EDMF scheme performs quite well over the region depicted in Figure S2 of the Supporting Information S1 because it shows relatively narrow distributions, and its median values compare closely to the observations. In contrast, the other three WRF configurations show much broader distributions that are not evident in the satellite retrievals.
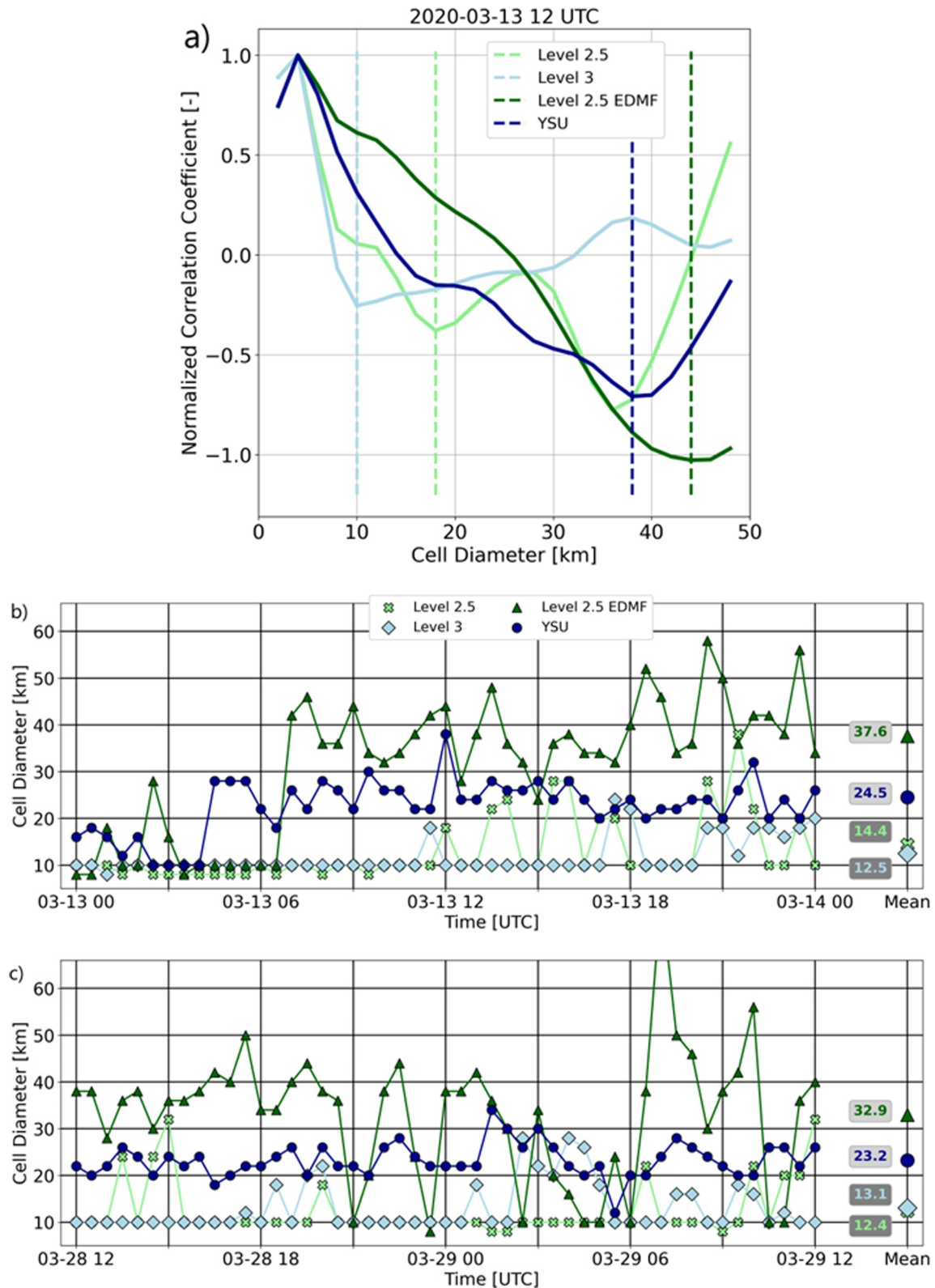
Figure 3. (a) Snapshots at 12 UTC on 13 March of convective cell size determined via the 100 m AGL horizontal convergence field. A two-point correlation method is applied to the convergence field, with the local minimum of the normalized correlation coefficient representing the cell radius. Here, we adjust the x-axis scale so that the minimum corresponds with the cell size. (b and c) Time series of cell size for the four WRF configurations, computed via the method illustrated in (a). The mean values over the time period are shown at the end of the time series, with the 13 March case computing the mean beginning at 06 UTC once cellular convection begins in all simulations.

3.4. Bottom-Up Perspective From AMF1

The large number of ground-based instruments deployed during the COMBLE field project at AMF1 afford us the opportunity to examine a number of key cloud properties during the two CAO events. To provide a visual representation of the convective cell structure as seen by the profiling AMF1 instruments during the 13 March case, we plot observed reflectivity from the KAZR in addition to forward-simulated reflectivity produced by CR-SIM from the WRF virtual tower outputs (Figure 5). During this 6 hr period, the measurements show a variety of cloud structures, including both isolated and merged or multi-cells (Figure 5f). In the first hour, a multi-cellular cloud structure is observed, followed by clear sky and several single cells that are either clearly distinct or loosely connected. In general, the cloud tops within the ∼10–25 dBZ cores are quite deep, ranging from ∼3.5–5 km. Through CR-SIM's forward simulation from the four WRF configurations (Figures 5a–5d), it is apparent that the model can simulate cellular-like features characterized by varying widths, depths, and intensities. Resolving the microscale structures observed by the KAZR is not possible for our WRF mesoscale configuration given the model's effective resolution (∼6Δ = 6 km or ∼10 min temporal resolution assuming mean background wind of 10 m s^{-1}). Therefore, we time-average the KAZR observations to 5 min (Figure 5e) based on qualitative comparison with WRF. We also time-averaged the raw data to 1, 2, and 10 min, but these produced less desirable results (not shown). The Level 2.5 EDMF scheme clearly produces the widest and deepest cells. By the end of this 6 hr period, all of the simulations produce too much condensate near cloud top, which is manifested as moderately low reflectivity values (∼−25 to −10 dBZ).

Time series traces of the column maximum reflectivity along the time-height plot shown in Figure 5, as well as traces of observed and simulated CTT, cloud top height (CTH), and liquid water path (LWP), can be seen in Figure 6. We also show a 6 hr period from the 28 March case for comparison. Overall, WRF captures the range and periodicity of column maximum reflectivity quite well for this 6 hr time period in both cases, with some overprediction for the 28 March event. In general, we do not expect the model to reproduce the exact timing of individual cells considering their transient nature when passing over the AMF1 site. The CTT traces from WRF show good agreement with some overestimation (i.e., warmer CTTs) for both cases, which is also evident in the CTH plots as an underestimation. Given the very cold CTTs observed and modeled during both events, one may expect homogeneous freezing to occur. We note that the Thompson Aerosol-Aware microphysics scheme allows for homogeneous freezing of deliquesced aerosols and liquid water drops at temperatures colder than −35 °C (Koop et al., 2000) and −38 °C (Bigg, 1953), respectively. Lastly, both the observations and simulations of LWP highlight the substantial liquid production in the cloud cores, with values approaching 1,000 g m^{-2} in the mature cells. Interestingly, the robust cell passing the AMF1 near 14:20 UTC on 13 March (cf. Figures 5e and 5f) does not contain much liquid, likely because it is glaciated and in a decaying stage (e.g., Geerts et al., 2022). Compared to the microwave radiometer's LWP measurements, the WRF simulations show a reasonable range of LWP values, albeit underestimating the most intense LWP values in the 13 March case and missing a high LWP period from ∼4–5 UTC in the 29 March case.

In Figure 7, we more quantitatively evaluate the individual WRF configurations for these four parameters by considering AMF1 observations during the two CAO cases when convective cells were observed. The distributions and boxen plots confirm that the model generally performs well for the column maximum reflectivity during the 13 March case (Figure 7a); however, all simulations overestimate maximum reflectivity for the 28 March case (Figure 7e). YSU matches the observations of maximum reflectivity most closely for both cases. Overall, WRF simulates CTT (Figures 7b and 7f) and CTH (Figures 7c and 7g) reasonably well, with the Level 2.5 EDMF scheme being the outlier (i.e., producing relatively deeper clouds and thus colder CTTs). It is worth noting that the EDMF approach does not as clearly produce the best results when compared to the AMF1 observations, which is in contrast to our findings using the satellite measurements of CTT (cf. Figure 4). We can attribute this apparent inconsistency to three potential factors: (a) we consider a spatial domain with the satellite versus a single point at AMF1; (b) differences in the CTT retrieval method from the KAZR and satellite; (c) the satellite's nominal resolution of 375 m is insufficient to capture the cloud edge features, which is likely where the lowest CTHs and thus warmest CTTs occur. While this discrepancy certainly deserves further attention, additional investigation is out of the scope of the present work. Finally, we find that the model consistently underestimates LWP for the 13 March case (Figure 7d) and reasonably well simulates LWP in the 28 March case (Figure 7h) despite the overestimation in maximum reflectivity.
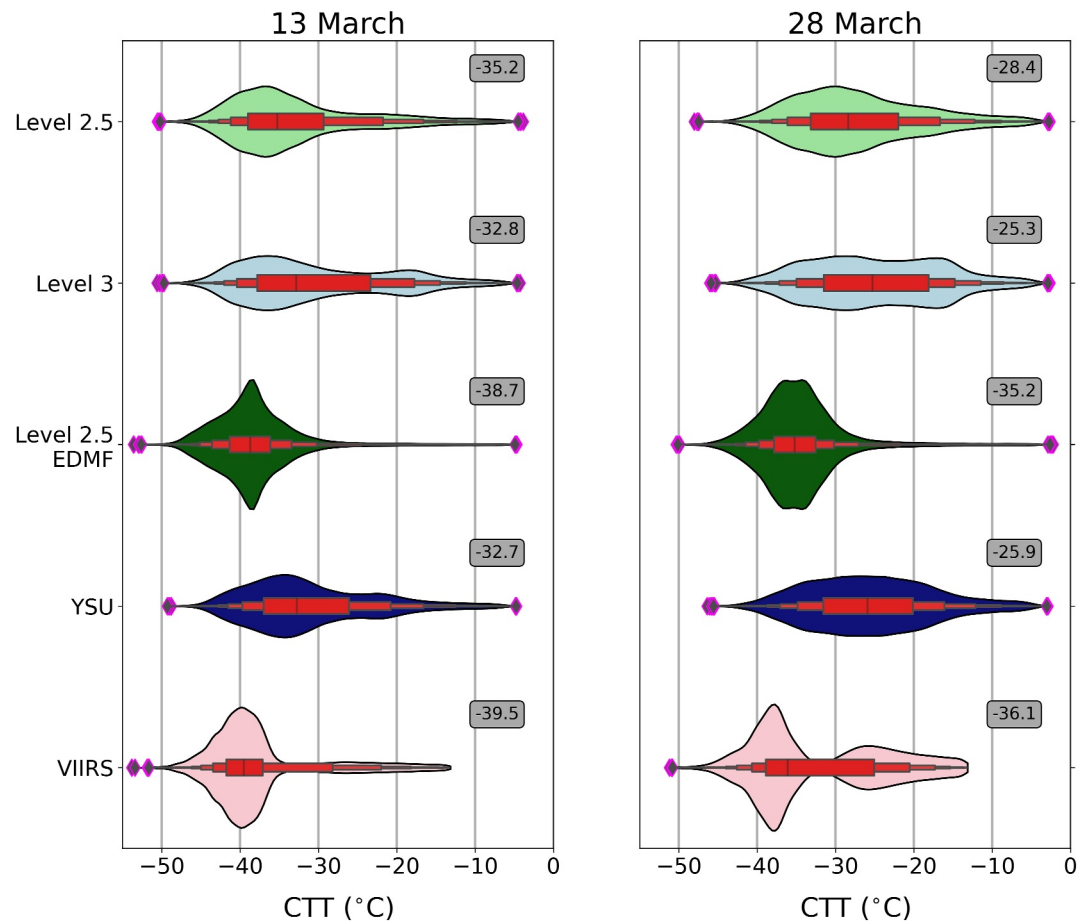
Figure 4. Distributions and boxen plots of CTT for (left) 13 March and (right) 28 March CAO cases. The gray boxes show the median value for each distribution. For each case, we combine all NOAA-20 VIIRS and SNPP VIIRS scenes and compare to the WRF simulations using the closest WRF output time. See Section 2.4 for details about the model-observation evaluation.

3.5. Clarifying the Role of Parameterized Mass-Flux

Thus far, we have presented results comparing the four selected PBL parameterizations. To a first order, the high-resolution mesoscale simulations are able to capture the general cloud characteristics and mesoscale organization. Perhaps the most striking result is that the Level 2.5 EDMF scheme clearly produces the widest and deepest cells, and thus those with the coldest CTTs. In this section, we seek to better understand the role of the non-local MF component of the scheme, whose purpose is to represent the vertically coherent convective structures that are ubiquitous under intense CAO conditions.

In Figure 8, we compare various components of the ED parameterization from the Level 2.5 (panels a, b, c) and Level 2.5 EDMF (panels d, e, f) simulations. Panels (a, d), (b, e), and (c, f) show parameterized quantities: TKE, vertical momentum flux terms, and buoyancy flux terms, respectively. Other plotted variables are described in the figure caption. Any differences between the two schemes is due solely to the mass-flux component of EDMF. These cross-sections are taken at the same time as Figure 2 along the dashed green lines. We select cross-sections such that they cut through well-defined cells in each simulation, based on the various parameters plotted in Figure 2. Hence, the cross-section locations are different for the two simulations.

For both the Level 2.5 and Level 2.5 EDMF models, the largest values of parameterized TKE are confined to the lowest ~1,000 m, with regions of enhanced TKE seen in fingers extending to ~2,500 m (Figures 8a and 8d), not in the echo tops which extend twice as high. Vertical momentum fluxes are largest at the cold pool edges due to the convergence patterns (cf. Figure 2) and strong vertical gradients in the u- and v-wind components (Figures 8b and 8e) which imply strong vertical motions.
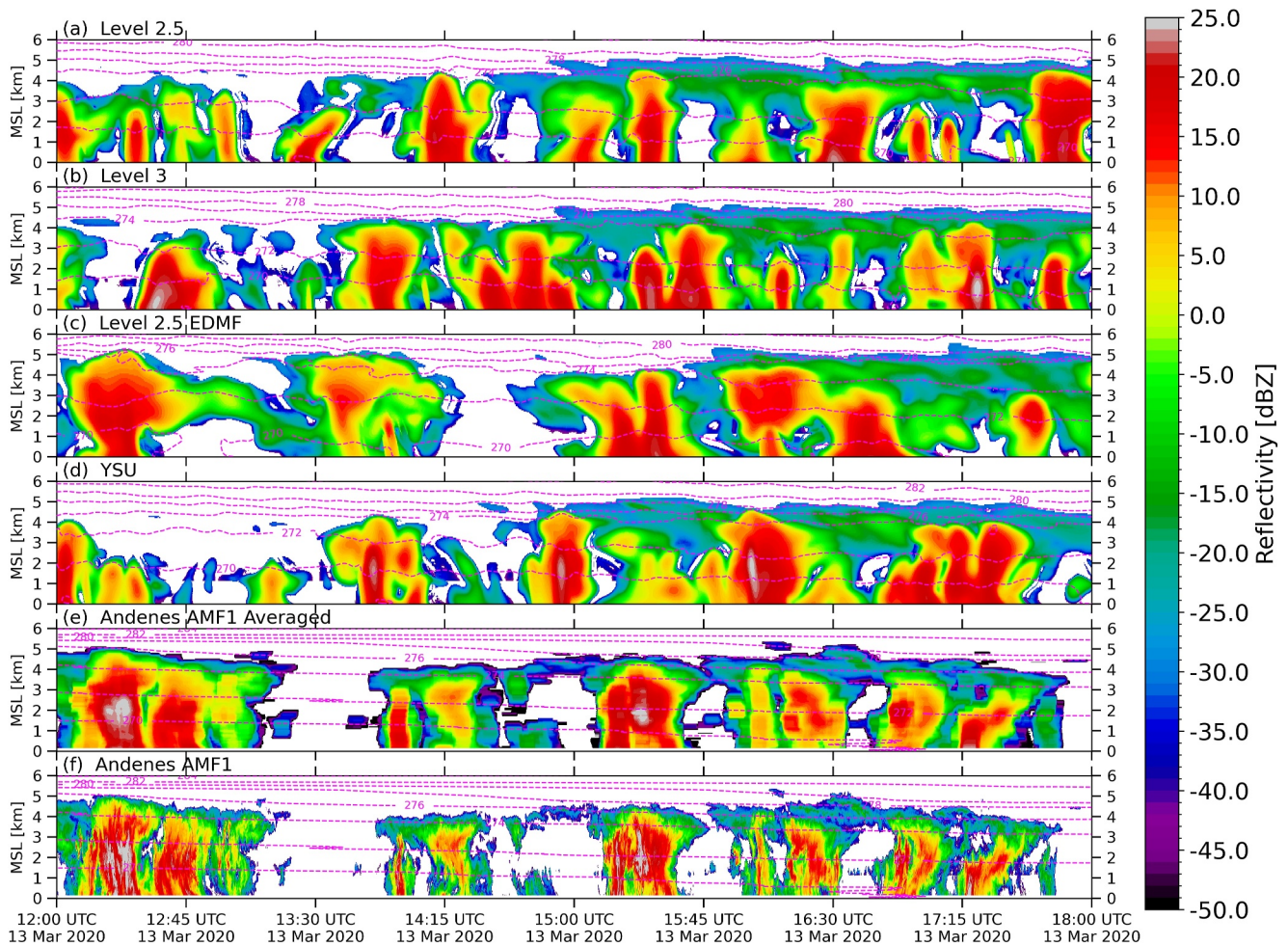
Figure 5. Time-height comparison of (a–d) modeled KAZR reflectivity (6 s time resolution) generated by the CR-SIM forward simulator and (e and f) observed KAZR reflectivity for a 6 hr period during the 13 March event according to the colorbar. Panel (e) shows the observed KAZR reflectivity time-averaged to 5 min to better compare with WRF, while panel (f) shows the raw (4 s time resolution) observed KAZR reflectivity. Potential temperature contours (every 2 K) are shown in magenta.

In the surface layer (lowest few 100s of m), the relatively warm SSTs generate positive buoyancy fluxes (Figures 8c and 8f). Plumes of strong negative buoyancy fluxes arise in the updrafts above the surface layer, indicating entrainment and/or overshooting. The vertical buoyancy flux convergence implies intense turbulent heating near the base of the updrafts. Cold pools tend to suppress the layer of positive buoyancy fluxes near the surface. Horizontal gradients arising from the presence of cold pools and narrow updrafts are likely non-negligible at the present Δ, highlighting the potential benefit of using a 3D PBL parameterization (Juliano, Kosović, et al., 2022).

In both configurations, there is a clear linkage between the dynamics, turbulence, and microphysics. Updraft regions develop at cold pool edges (Figures 8b and 8e) due to the aforementioned convergence patterns, and, within these updrafts, we find the presence of cloud liquid water that oftentimes coexists with ice crystals or snow (Figures 8a and 8d). Shafts of falling snow, associated primarily with downdraft regions, extend to the surface in accordance with the cold pools. The Level 2.5 EDMF model produces more robust vertical motions than the Level 2.5 model (Figures 8c and 8f), which may explain the generally higher frequency of frozen condensate, especially near cloud top.

We more explicitly probe the role of the MF component of the EDMF scheme by plotting in the same cross-section its fractional area (A_{EDMF}), vertical velocity (W_{EDMF}), and total parameterized convective scalar flux (only positive values of M_i; cf. Equation 7) (Figure 9). These parameters are critical to the MF scheme (cf. Equations 6 and 7). As expected, the MF parameterization is most active in regions of relatively weak resolved
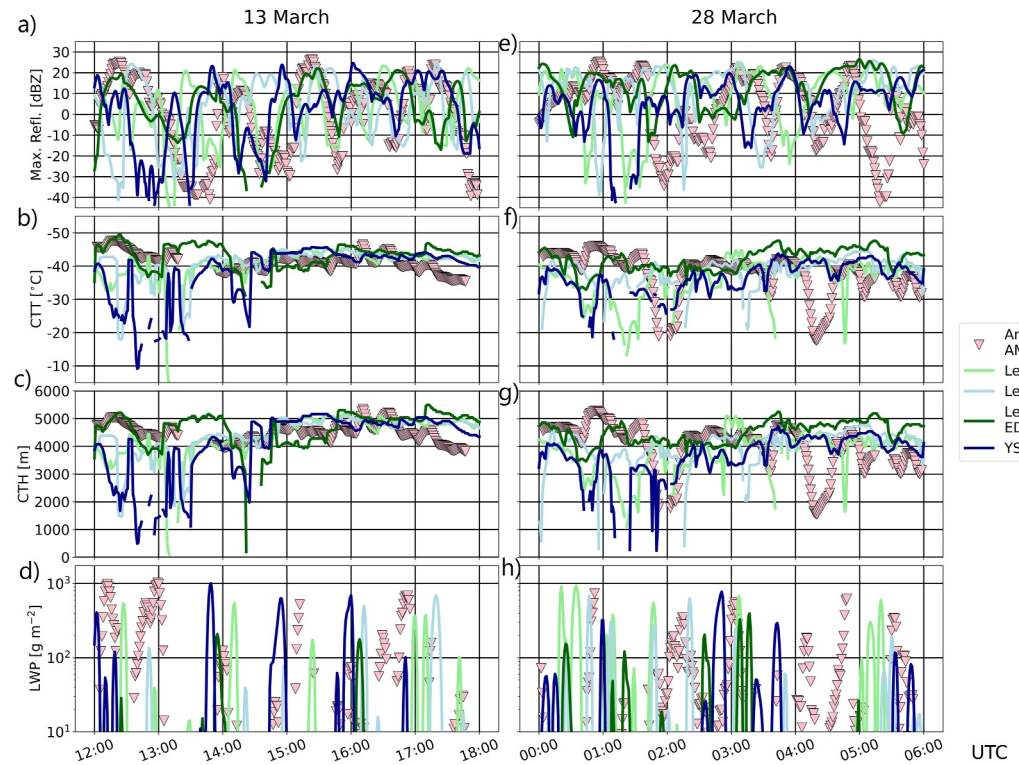
Figure 6. Time series of observed and modeled (a, e) maximum columnar reflectivity, (b, f) CTT, (c, g) CTH, and (d, h) LWP for select 6 hr periods during the (a, b) 13 March and (e–h) 28 March cases. Note that LWP values <30 g m^{-2} are shown purely for visual purposes and are not included in the quantitative analysis in Figure 7.

vertical motions, especially with respect to the updrafts. A_{EDMF} is largest near the surface and decreases with height (Figure 9a). The maximum A_{EDMF} value (=0.1; cf. Section 2.3.2) appears to be reached in many locations near the surface. Meanwhile, W_{EDMF} generally increases with height, and maximum values commonly exceed 2 m s^{-1}, signifying the intense convective motions that remain parameterized at $\Delta = 1$ km (Figure 9b). Multiplying A_{EDMF} and W_{EDMF} leads to the total parameterized convective scalar MF for all subgrid-scale plume sizes (Figure 9c). As a result, this field follows closely with the previous two fields, and it illustrates the regions of the cloud system impacted most by the MF part of the EDMF scheme.

It is evident that the MF scheme is active in columns extending from the surface to near the cloud top (~3,500 m), suggesting that the cells in intense CAO conditions are tightly linked to the surface through BL-spanning eddies. Thus, the role of the non-local aspect of the Level 2.5 EDMF scheme is non-negligible in this environment. As latent heat is released through phase changes of water, the updrafts produced by the MF scheme are maintained well above the surface and can extend to near the cloud top. We suspect that additional buoyancy contribution from the MF scheme may be the reason for the EDMF scheme producing deeper clouds relative to the ED scheme. However, given that our findings suggest that the EDMF approach produces cloud structures that are too deep at Andenes, perhaps because the WRF implementation of MYNN EDMF has not been tuned for CAO conditions (to be discussed in Section 4), it is likely that the MF scheme is overactive for these two CAO cases and at $\Delta = 1$ km.

3.6. Airmass History

Our analysis has focused on the cellular cloud characteristics at Andenes, which is located ~1,000 km downstream of the pack ice edge. To more clearly understand the airmass history during the 13 March case from a Lagrangian perspective, we conduct a backward trajectory analysis. A trajectory is launched from Andenes beginning at 12 UTC on 13 March at an altitude of 1 km using ERA5 Reanalysis (Figure 10a). The backward trajectory shows a nearly identical path for 0.5, 1, and 2 km starting altitudes (not shown). In Figures 10b–10d, we show the simulated instantaneous mean surface precipitation rates along the trajectory for rain, snow, and graupel, respectively, for each simulation since precipitation has been shown to initiate the breakup of overcast conditions
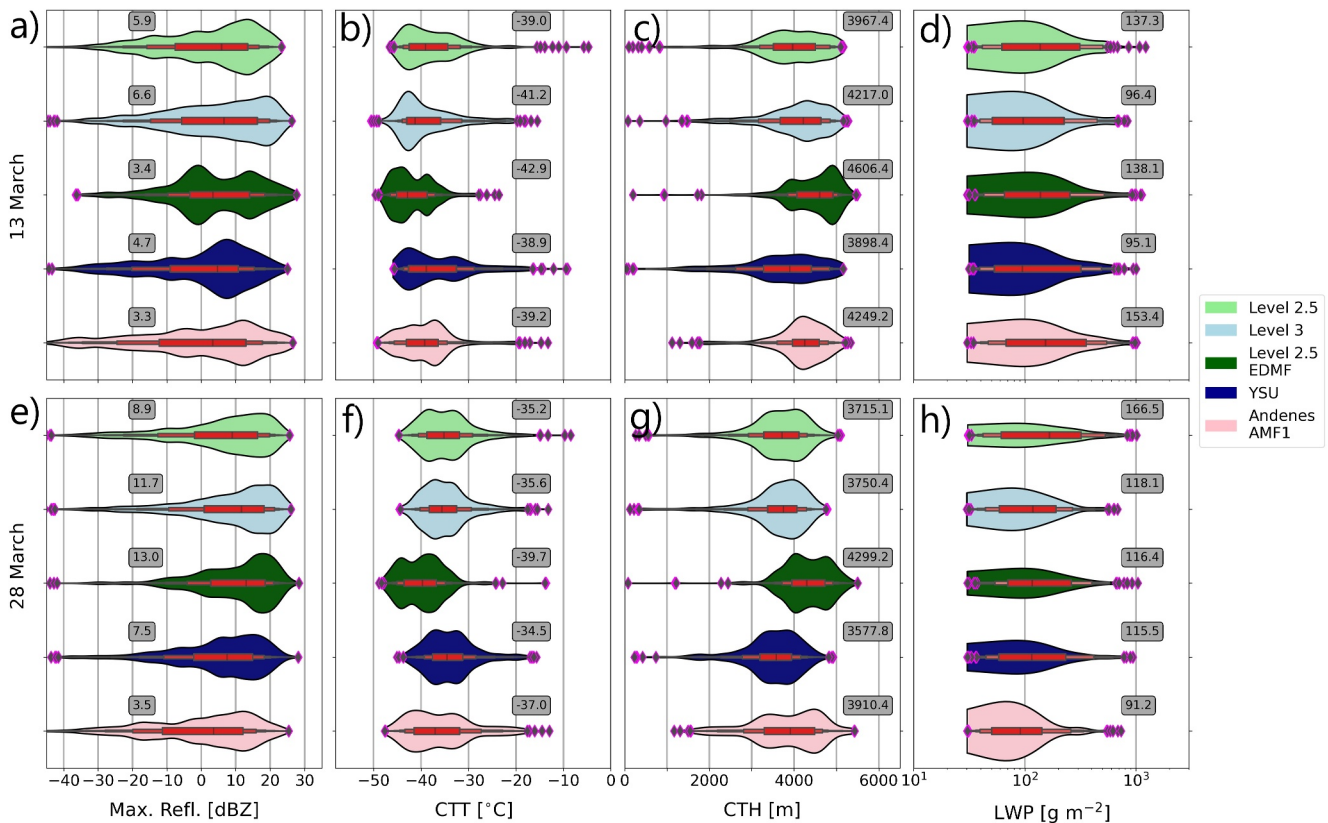
Figure 7. Distributions and boxen plots of (a), (e) maximum columnar reflectivity, (b, f) CTT, (c, g) CTH, and (d, h) LWP for the entirety of the (a, b) 13 March and (e–h) 28 March cases. The gray boxes show the median value for each distribution. Both observations and model results are time-averaged to 1-min for CTT, CTH, and LWP. For the maximum reflectivity, raw KAZR observations (linear Z units) are time-averaged to 5-min.

in CAO MPCs (e.g., Abel et al., 2017; Tornow et al., 2021). Evident is the marked relative increases in rain and especially graupel precipitation rates beginning approximately 8 hr before the airmass arrives at Andenes. The Level 2.5 EDMF scheme produces the largest precipitation rates for these two categories. Nonetheless, for the entire 16 hr period, the snowfall rates dominate the total precipitation rate, and their magnitudes are rather constant, increasing slightly from −16 to 0 hr. The Level 3 scheme simulates the highest snowfall rate and thus total precipitation rate out of all four WRF configurations. We note that laser disdrometer measurements at AMF1 show a mix of rain, snow, and graupel for our CAO events, although the relative frequencies are uncertain (Appendix A in Mages et al. (2023)).

Commensurate with the notable increase in rainfall and graupel precipitation rates as the airmass approaches Andenes is the increase in the fraction of model grid cells where rainfall and graupel precipitation occurs (Figures 10e–10g). Meanwhile, during this time, the fraction of grid cells with snowfall decreases drastically, suggesting cloud breakup, and the transition to open cellular clouds. This breakup appears to occur soonest (latest) in the Level 2.5 (Level 2.5 EDMF) scheme, with the most rapid decrease in the snowfall area occurring once both rainfall and graupel precipitation rates and fractional coverage ramp up. Given that snowfall precipitation rates increase slightly over time, this points toward snowfall becoming more concentrated during this transition. Our results suggest a linkage between cloud breakup and precipitation processes, corroborating previous studies.

Mean vertical profiles of the five hydrometeor categories represented in the Thompson-Eidhammer microphysics scheme are plotted at 12, 6, and 0 hr prior to the airmass arriving at Andenes (i.e., −12, −6, and 0 hr) in Figure 11. These three times represent conditions before, during, and after the cloud transition, respectively. Prior to the transition (Figure 11, top row), all four schemes show relatively little cloud liquid, no rain, and no graupel. The Level 2.5 EDMF scheme shows the deepest cloud layer (top near ∼3 km), while the other three schemes show a similarly deep cloud (top near ∼2 km). CCN concentration and cloud droplet number concentration (CDNC) range from ∼60–110 cm^{-3} to ∼10–60 cm^{-3}, respectively, in the BL depending on the PBL scheme (Figure S3 in
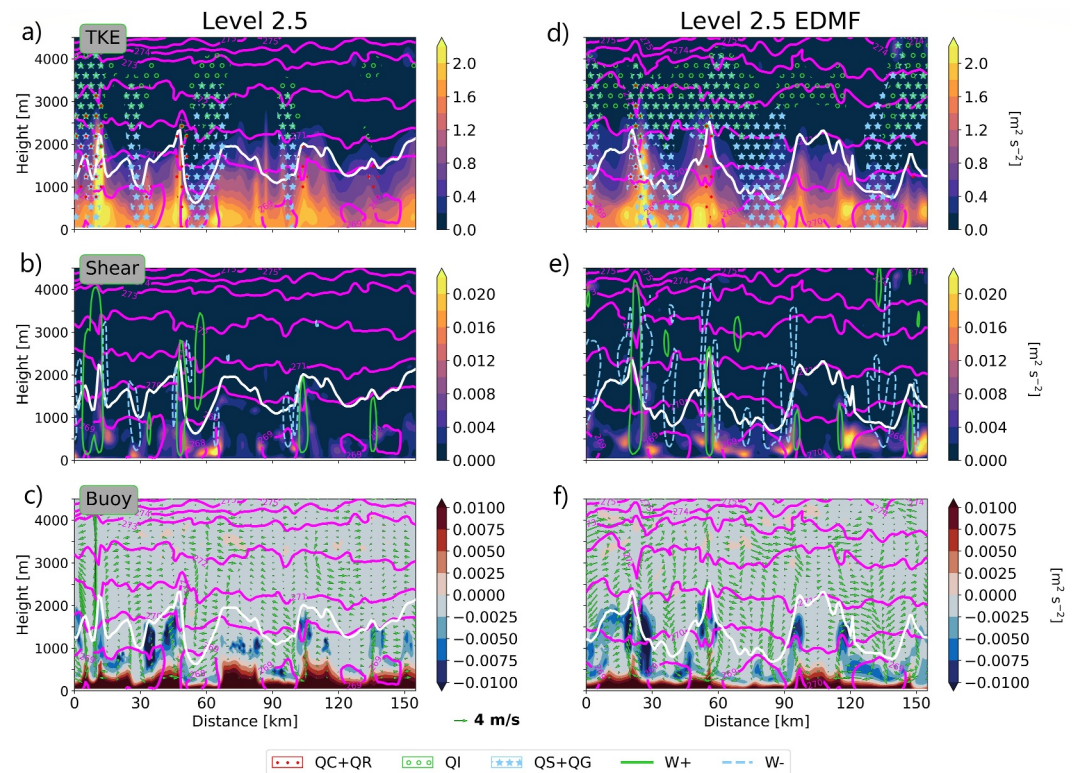
Figure 8. Vertical cross-sections of parameterized TKE for the (a) Level 2.5 and (d) Level 2.5 EDMF schemes. Also shown are the parameterized (b, e) vertical momentum and (c, f) buoyancy flux terms. Fields are contoured according to the respective colorbars. All panels show θ_v (magenta contours) and the BL height as diagnosed by the PBL scheme (white contour). In panels (a), (d) we show regions of the following mass mixing ratios: cloud liquid and rain (QC and QR; red dots; $>10^{-3}$ g kg^{-1}), cloud ice (QI; green circles; $>10^{-3}$ g kg^{-1}), and snow and graupel (QS and QG; blue stars; 10^{-1} g kg^{-1}). Substantial vertical motions (positive: solid green, negative: dashed blue; magnitude >0.5 m s^{-1}) are plotted in panels (b), (e), and x–z flow vectors are plotted in panels (c), (f) according to the arrow key.

Supporting Information S1). Cloud ice is generated in a layer above the cloud liquid and near cloud top, with the cloud ice mixing ratio several times larger in the Level 2.5 EDMF scheme compared to the other schemes. This behavior is due to an enhancement in ice number concentration in the Level 2.5 EDMF model (Figure S4 in Supporting Information S1). Snow dominates the cloud mass throughout the entire layer while falling to the surface in all schemes, with the Level 3 scheme showing the largest mixing ratios.

During the cloud transition, the cloud layer has deepened by ~1 km in all simulations (Figure 11, middle row). Moreover, the production of cloud liquid increases in all schemes, leading to the initiation of rain processes, and the peak altitude and mixing ratio of cloud liquid is noticeably lowest in the Level 3 scheme. The substantial decrease in both CCN concentration and CDNC between −12 and −6 hr (Figure S3 in Supporting Information S1), in addition to the increase in LWP, likely triggers the onset of rain (see also Tornow et al., 2021, 2023). Cloud ice mixing ratios are similar as in −12 hr for Level 2.5 EDMF and slightly higher (lower) for Level 2.5 and YSU (Level 3). At this time, the ice number concentration has increased in all simulations except for the Level 3 scheme (Figure S4 in Supporting Information S1). It is worth noting that cloud top in the Level 2.5 EDMF scheme is deep enough for homogeneous freezing of both deliquesced aerosols and liquid water drops. The Level 3 scheme still shows the largest snow mixing ratios below ~2 km altitude. By this time, graupel is generated in all schemes, with Level 2.5 EDMF and Level 2.5 showing the largest mixing ratios.

Once the airmass reaches Andenes, the cloud layer has deepened once again by ~1–1.5 km (Figure 11, bottom row). The liquid cloud layer is maintained due to enhanced vertical motions in the low-level convergence regions (cf. Figure 8). Production of both rain and graupel increase further, especially in the Level 2.5 EDMF scheme, which also shows a clear decrease in cloud ice mixing ratio and number concentration (Figure S4 in Supporting Information S1) as well as snow mixing ratio. All schemes show further losses in CCN concentration and CDNC
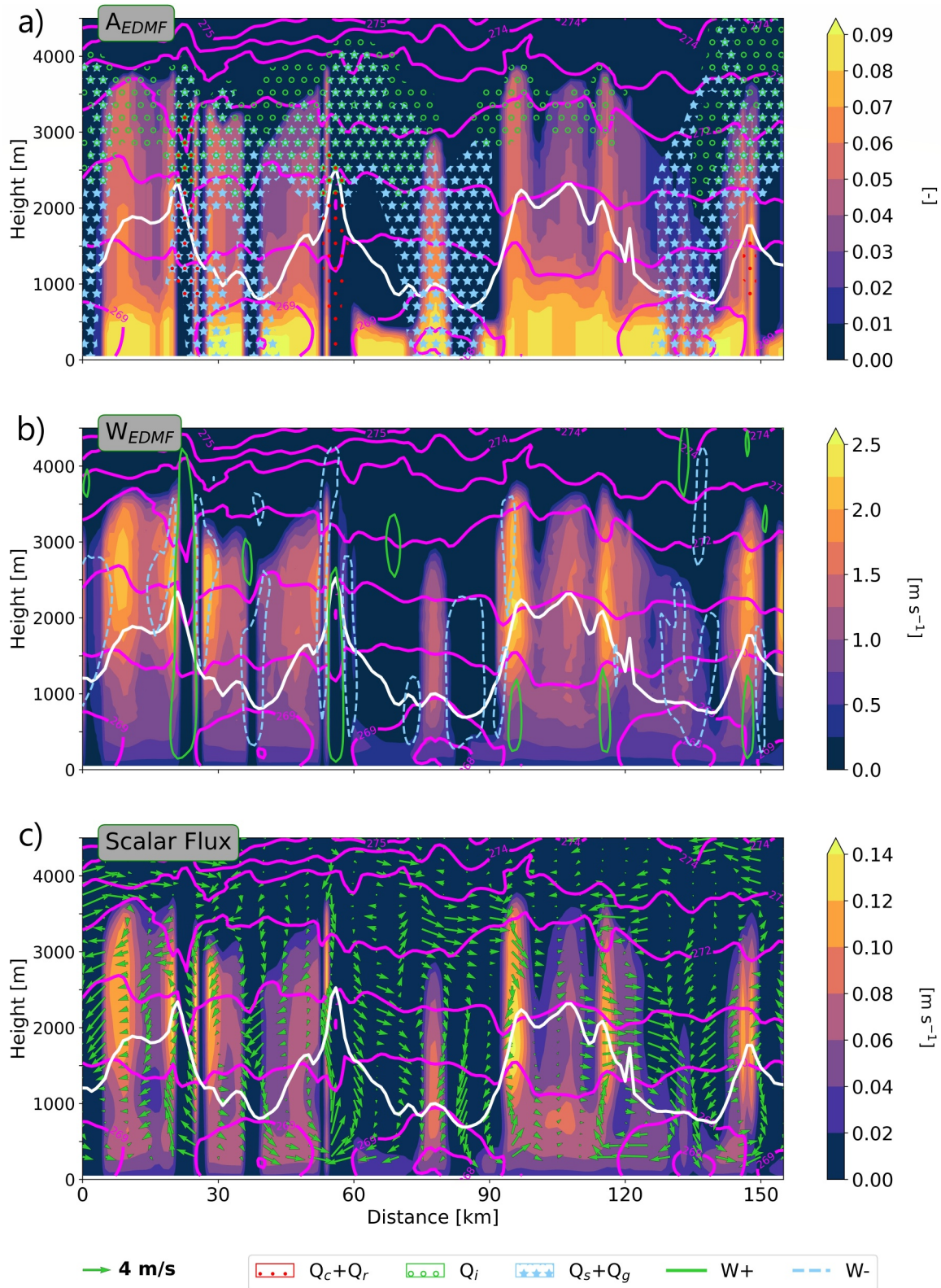
Figure 9. As in Figure 8, except showing parameterized EDMF parameters: (a) fractional area of updrafts, (b) updraft vertical velocity, and (c) total (positive) parameterized convective scalar flux. The fields are contoured according to the respective colorbars. Secondary fields are plotted in each panel as in Figure 8.
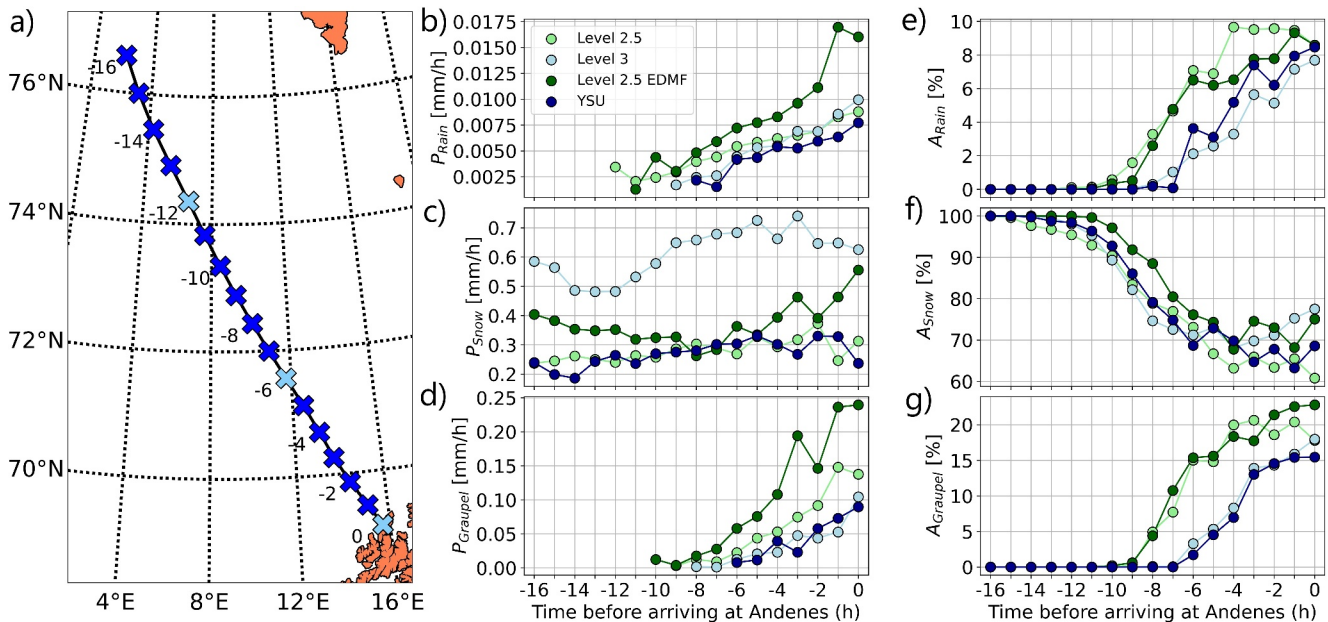
Figure 10. (a) Backward trajectory launched from Andenes, Norway at 12 UTC on 13 March and at an altitude of 1,000 m. Each "X" symbol represents the hourly location of the air parcel, with the numbers representing the time (hours) prior to the airmass arriving at Andenes. The light blue symbols show the location of air parcels examined in Figure 11. Also shown are time series of mean surface precipitation rates for (b) rain, (c) snow, and (d) graupel as well as fraction of model grid cells experiencing (e) rainfall, (f) snowfall, and (g) graupel (precipitation rate threshold of 0.001 mm/hr). At each time interval, a 50×50 km^2 box is drawn around the parcel location to compute the statistics shown in this figure and Figure 11.

between -6 and 0 hr (Figure S3 in Supporting Information S1). A cross-sectional view, shown in Figure S5 of the Supporting Information S1 and discussed in Text S2 of the Supporting Information S1, highlights the aerosol-cloud-precipitation interactions near Andenes.

We also examine $K_{v,h}$ and $K_{v,m}$ from the PBL schemes during this airmass transition (Figure 11, last two columns). These terms are important for dictating the strength of the subgrid-scale vertical mixing of heat and momentum, respectively (cf. Section 2.3.2). It is clear from Figure 11 that $K_{v,h}$ and $K_{v,m}$ values are at a maximum at -12 hr and decrease over time. The ratio of $K_{v,h}/K_{v,m}$ (i.e., inverse turbulent Prandtl number, Pr_t) is also plotted to highlight differences in vertical mixing of heat and moisture versus momentum between the PBL schemes. All simulations show $Pr_t^{-1} > 1$ near the surface as a result of buoyancy increasing the turbulent transfer of heat relative to that of momentum (e.g., Li, 2019). However, throughout the airmass transition, YSU models the largest Pr_t^{-1} values which remain above 1 until $\sim$2 km ASL, while Pr_t^{-1} in the other three schemes decreases rapidly below unity. Most notable is the sharp decrease at low levels in Pr_t^{-1} in the Level 3 scheme.

We believe this finding related to Pr_t is important because it may control the modeled convective structures (e.g., Ching et al., 2014) and, as a result, the cloud properties (e.g., Pithan et al., 2015). In this study, each of the PBL schemes to some extent rely on Pr_t. Recall that the vertical turbulent mixing of momentum and heat/moisture in the Level 2.5, Level 3, and YSU schemes strongly depends on $K_{v,m}$ and $K_{v,h}$. While these terms are also important for the Level 2.5 EDMF scheme, its vertical mixing of heat is also largely dependent upon the MF component, which is not affected by $K_{v,h}$ (cf. Equation 6). Further investigation is required to determine whether the relatively small Pr_t^{-1} values modeled by the Level 3 scheme are responsible for its lack of coherent convective cell structures (cf. Figures 2 and 3). Given our rather poor understanding of the impact of Pr_t on weather and climate in general (Li, 2019), future studies should more deeply focus on this topic.

4. Summary and Conclusions

In this study, we examine the horizontal and vertical cellular cloud structures and properties of two intense marine CAOs observed during the COMBLE field project in March 2020. Both cases were characterized by widespread, robust CAO conditions due to strong northerly flow through the Fram Strait and toward the main COMBLE site at
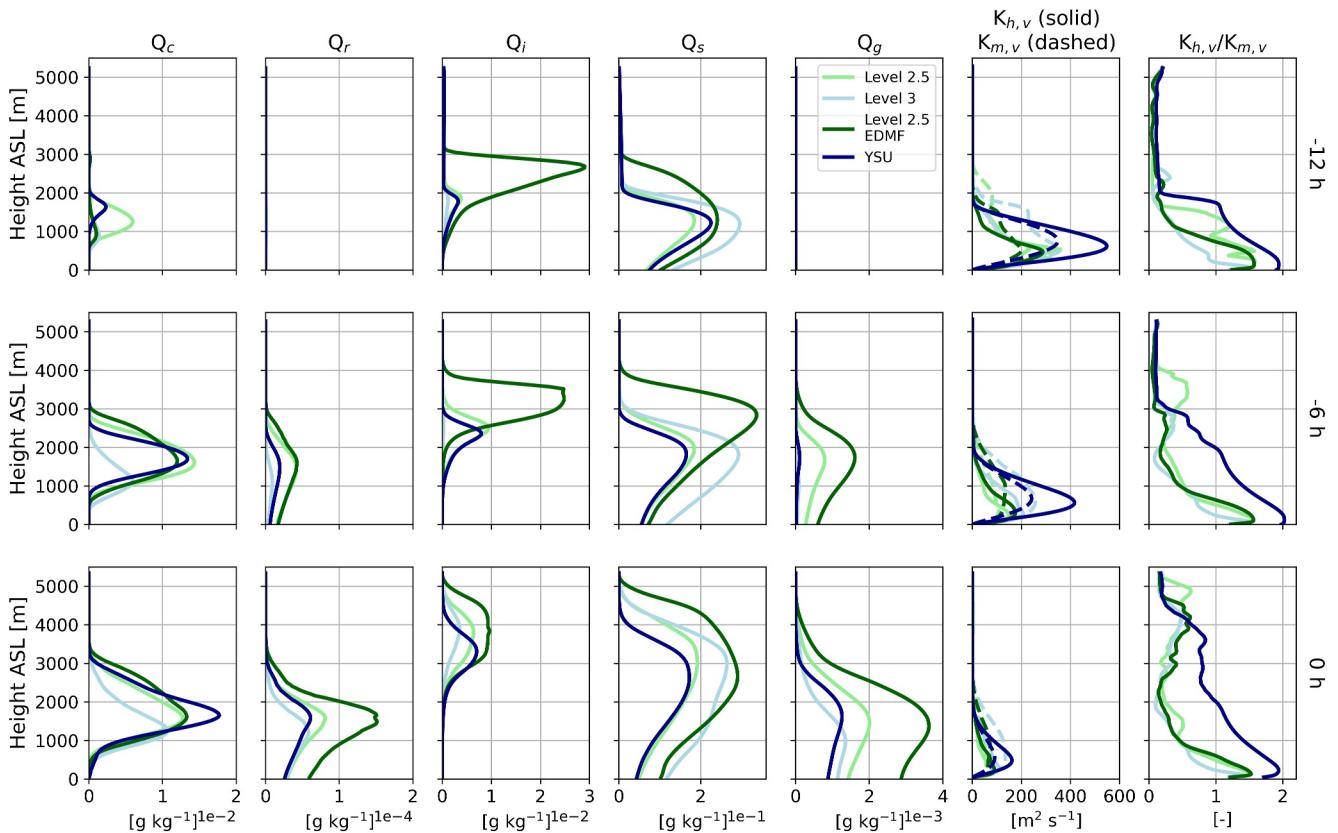
Figure 11. Vertical profiles of QC, QR, QI, QS, and QG mass mixing ratios at (top row) −12 hr, (middle row) −6 hr, and (bottom row) 0 hr prior to the 13 March airmass reaching Andenes. The location of the airmass at each of these times in indicated by the light blue symbols in Figure 10a. We note that the x-axis scales are different.

Andenes, Norway, where the AMF1 measurements were collected. The suite of instruments at AMF1 enables us to deeply examine the vertical cloud morphologies as well as the microphysical and macrophysical properties of these MPCs. VIIRS satellite retrievals of CTT are used to supplement the AMF1 measurements across a broader geographical area offshore Andenes. To better contextualize the observations, we conduct high-resolution mesoscale simulations ($\Delta = 1$ km) using the WRF model. Given our relatively poor understanding of the impact of parameterized turbulence approaches on simulated CAO cloud properties, this study tests four different turbulence closure schemes within two commonly used PBL scheme frameworks: MYNN and YSU. Of particular importance for the model-observation evaluation at AMF1 is the application of the CR-SIM forward-simulator on WRF outputs to directly compare the model to the KAZR measurements.

Main findings stemming from our study are as follows:

- As modeled by WRF, convective cells near Andenes are defined by coherent patterns of low-level convergence and mid-BL vertical motions that arise in response to the development of cold pools.
- A two-point correlation method applied to the divergence field yields cell sizes ranging from ~12–38 km depending on the turbulence closure approach (compared to ~20–25 km observed), with the YSU and Level 2.5 EDMF scheme producing the largest, and most reasonable, cell sizes.
- VIIRS satellite retrievals of CTT suggest that all model configurations, except for EDMF, overestimate CTT (i.e., median distribution cloud tops are too warm by up to ~30%), with EDMF agreeing quite well overall (within ~2.5% bias).
- Meanwhile, WRF simulations show generally better agreement with CTT measured at the AMF1 site (within ~10% bias), pointing to the utility of applying the CR-SIM forward-simulator to model outputs. Compared to the AMF1 measurements, the EDMF scheme simulates clouds that are too deep and too cold.
- At Andenes, WRF tends to overestimate maximum reflectivity—especially for the 28 March case—and underestimate cloud top height (except for EDMF, which overestimates cloud top height). The variability

and peak values in LWP are predicted well, with slight biases of opposite sign for the two cases and no clear dependence on turbulence closure method.

- Vertical cross-sections through the simulated cellular structures reveal the secondary circulations and mixed-phase nature of the CAO clouds, with liquid production in updrafts that form at cold pool edges and falling snow and graupel in downdraft regions. Shear and buoyancy production of turbulence patterns are related to the cold pool structure.
- The MF component of the EDMF scheme is found to be quite active (MF > 0.1 m s^{-1}) in broad columns stretching from the surface to ∼3.5 km ASL, suggesting that BL-spanning eddies are important for the life-cycle of convective clouds under CAO conditions.
- Extraction of model outputs along backward trajectories launched at the AMF1 site reveal that all model configurations simulate increases in precipitation rates and fractional coverage that are correlated with the timing of cloud breakup.
- The magnitude of Pr$_t$ relative to unity, which controls the relative strengths of subgrid-scale vertical heat and momentum transfer in the BL, may play an important role with respect to mesoscale cloud organization. We find that the Level 3 scheme shows the largest values of Pr$_t$, possibly leading to less coherent cellular structures.

In this region of the world, MPCs in the form of open cells typically form only during strong CAO conditions (widespread MCAO ≥ 8 K) with long fetch (∼1,000 km). We expect that an intense CAO with long fetch will initially form convective rolls that transition to closed cells and then open cells far downstream that have broadly similar characteristics as those seen here. Thus, we believe that our two cases are representative of strong CAO cases whether in the present or future climate. Moreover, we expect that the differences in representation of physical processes between the schemes would generally hold true for the more common but weaker CAO cases. However, we suspect that these two intense cases, with cloud tops approaching 4–5 km, lie on the edge of conditions for which a traditional 1D PBL scheme has been designed. We can identify two key differences between weak and strong CAO cases in the context of this study. First, the size of BL-spanning eddies that are still present by the time the airmass has reached Andenes. These are generally constrained by the BL depth, which is more typically 1–2 km under weaker CAO conditions (as opposed to 3–5 km under the stronger CAO conditions). Because the MF scheme likely will play a smaller role during a weaker case (i.e., the non-local component of the parameterized mixing diminishes), a user may get away with using a local PBL scheme to represent vertical turbulent exchanges in CAO cloud layers. Second, the very cold cloud tops in the two intense cases examined here allowed for homogeneous freezing to occur, which may feedback on the open cell lifecycle and thus impact the PBL scheme through latent heat release. This primary ice production mechanism through freezing of drops is unlikely to be active when the cloud tops are 1–2 km, further supporting the notion that a local PBL scheme may be more appropriate under weak CAO conditions than strong CAO conditions. However, we emphasize that when non-local mixing is present under convective conditions, such as in CAOs, it must be represented if one intends to accurately represent the total amount of vertical mixing.

One key outcome of our study is the apparent overactive behavior of the MF component of the MYNN scheme. Given that here we examine intense CAOs with a deep, yet rather ill-defined, BL characterized by relatively strong vertical motions by the time the airmass reaches Andenes, this likely represents a challenging scenario for the MF scheme. Moreover, our inner domain Δ falls within the turbulence gray zone, where the largest eddies become partially resolved; thus, the parameterized turbulence should be tapered to some degree. Future studies should explore the impact of making various aspects of the MF scheme more scale-aware to perhaps weaken the updrafts, which are likely too strong in the two cases examined here.

Within the context of our modeling configuration, especially related to the selected Δ, none of the schemes stand out as the clear winner (though Level 3 is clearly unsuitable). However, we believe that both the non-local Level 2.5 EDMF and YSU closure approaches are most suitable for simulating intense CAOs. Both schemes, which attempt to parameterize the effects of turbulent vertical mixing by large eddies on BL dynamics and clouds, produced the most reasonable cell sizes and agreed well with COMBLE measurements. The Level 2.5 scheme is likely a fine option if CAO conditions are less intense and a non-local approach is less warranted. This study highlights that turbulence closure scheme performance in the gray zone should be studied further. To help facilitate such understanding, our research group has conducted a realistic multiscale simulation with a domain spanning from the ice edge to Andenes and resolved at Δ = 150 m using the large-eddy simulation method. These model outputs may be used to more confidently understand CAO cloud lifecycles including turbulence exchanges affecting BL growth, precipitation processes, and cloud transitions.

Data Availability Statement

COMBLE campaign data at the Andenes site used in this study are available through the references listed in Section 2.1. VIIRS satellite imagery used in this study may be downloaded from the NASA Earthdata archive (https://www.earthdata.nasa.gov/). The WRF model code used in this study is public and may be found on the WRF GitHub repository (https://github.com/wrf-model). Files related to the WRF model setup, raw and post-processed WRF outputs, satellite retrievals, and analysis scripts are available in a Harvard Dataverse repository (https://doi.org/10.7910/DVN/U3VI1X; Juliano & Lackner, 2024).

References

Abel, S. J., Boutle, I. A., Waite, K., Fox, S., Brown, P. R. A., Cotton, R., et al. (2017). The role of precipitation in controlling the transition from stratocumulus to cumulus clouds in a Northern Hemisphere cold-air outbreak. *Journal of the Atmospheric Sciences*, *74*(7), 2293–2314. https://doi.org/10.1175/jas-d-16-0362.1

Angevine, W. M., Olson, J., Gristey, J. J., Glenn, I., Feingold, G., & Turner, D. D. (2020). Scale awareness, resolved circulations, and practical limits in the MYNN-EDMF boundary layer and shallow cumulus scheme. *Monthly Weather Review*, *148*(11), 4629–4639. https://doi.org/10.1175/mwr-d-20-0066.1

Bigg, E. K. (1953). The formation of atmospheric ice crystals by the freezing of droplets. *Quarterly Journal of the Royal Meteorological Society*, *79*(342), 510–519. https://doi.org/10.1002/qj.49707934207

Bogenschutz, P. A., & Krueger, S. K. (2013). A simplified PDF parameterization of subgrid-scale clouds and turbulence for cloud-resolving models. *Journal of Advances in Modeling Earth Systems*, *5*(2), 195–211. https://doi.org/10.1002/jame.20018

Bou-Zeid, E., Anderson, W., Katul, G. G., & Mahrt, L. (2020). The persistent challenge of surface heterogeneity in boundary-layer meteorology: A review. *Boundary-Layer Meteorology*, *177*(2–3), 227–245. https://doi.org/10.1007/s10546-020-00551-8

Brümmer, B., & Pohlmann, S. (2000). Wintertime roll and cell convection over Greenland and Barents Sea regions: A climatology. *Journal of Geophysical Research*, *105*(D12), 15559–15566. https://doi.org/10.1029/1999jd900841

Ching, J., Rotunno, R., LeMone, M., Martilli, A., Kosović, B., Jiménez, P. A., & Dudhia, J. (2014). Convectively induced secondary circulations in fine-grid mesoscale numerical weather prediction models. *Monthly Weather Review*, *142*(9), 3284–3302. https://doi.org/10.1175/mwr-d-13-00318.1

Clothiaux, E. E., Miller, M. A., Perez, R. C., Turner, D. D., Moran, K. P., Martner, B. E., et al. (2001). *The ARM millimeter wave cloud radars (MMCRs) and the active remote sensing of clouds (ARSCL) value added product (VAP) (DOE/SC-ARM/VAP-002.1).* ARM User Facility, Pacific Northwest National Laboratory. https://doi.org/10.2172/1808567

Crewell, S., & Löhnert, U. (2003). Accuracy of cloud liquid water path from ground-based microwave radiometry 2. Sensor accuracy and synergy. *Radio Science*, *38*(7–1). https://doi.org/10.1029/2002rs002634

Dahlke, S., Solbés, A., & Maturilli, M. (2022). Cold air outbreaks in Fram Strait: Climatology, trends, and observations during an extreme season in 2020. *Journal of Geophysical Research: Atmospheres*, *127*(3), e2021JD035741. https://doi.org/10.1029/2021jd035741

de Roode, S., Frederikse, T., Siebesma, A. P., Ackerman, A. S., Chylik, J., Field, P. R., et al. (2019). Turbulent transport in the gray zone: A large eddy model intercomparison study of the CONSTRAIN cold air outbreak case. *Journal of Advances in Modeling Earth Systems*, *11*(3), 597–623. https://doi.org/10.1029/2018ms001443

de Roode, S., Siebesma, A. P., Jansson, F., & Janssens, M. (2022). Dependency of mesoscale organization on grid anisotropy in large-eddy simulations of convective boundary layers at gray zone resolutions. *Journal of Advances in Modeling Earth Systems*, *14*(11), e2022MS003095. https://doi.org/10.1029/2022ms003095

Dudhia, J. (1989). Numerical study of convection observed during the winter monsoon experiment using a mesoscale two-dimensional model. *Journal of the Atmospheric Sciences*, *46*(20), 3007–3107. https://doi.org/10.1175/1520-0469(1989)046<3077:nsocod>2.0.co;2

Efstathiou, G. A. (2023). Dynamic subgrid turbulence modeling for shallow cumulus convection simulations beyond les resolutions. *Journal of the Atmospheric Sciences*, *80*(6), 1519–1545. https://doi.org/10.1175/jas-d-22-0132.1

Eirund, G. K., Possner, A., & Lohmann, U. (2019). Response of Arctic mixed-phase clouds to aerosol perturbations under different surface forcings. *Atmospheric Chemistry and Physics*, *19*(15), 9847–9864. https://doi.org/10.5194/acp-19-9847-2019

Fairless, T., Jensen, M., Zhou, A., & Giangrande, S. E. (2021). *Interpolated sounding and gridded sounding value-added products. No. DOE/SC-ARM-TR-183.* Pacific Northwest National Laboratory (PNNL). https://doi.org/10.2172/1248938

Field, P. R., Brozková, R., Chen, M., Dudhia, J., Lac, C., Hara, T., et al. (2017). Exploring the convective grey zone with regional simulations of a cold air outbreak. *Quarterly Journal of the Royal Meteorological Society*, *143*, 2537–2555. https://doi.org/10.1002/qj.3105

Fletcher, J., Mason, S., & Jakob, C. (2016). The climatology, meteorology, and boundary layer structure of marine cold air outbreaks in both hemispheres. *Journal of Climate*, *29*(6), 1999–2014. https://doi.org/10.1175/jcli-d-15-0268.1

Geerts, B., Giangrande, S. E., McFarquhar, G. M., Xue, L., Abel, S. J., Comstock, J. M., et al. (2022). The COMBLE campaign: A study of marine boundary layer clouds in Arctic cold-air outbreaks. *Bulletin America Meteorology Social*, *103*(5), E1371–E1389. https://doi.org/10.1175/bams-d-21-0044.1

Goger, B., Rotach, M. W., Gohm, A., Stiperski, I., Fuhrer, O., & de Morsier, G. (2019). A new horizontal length scale for a three-dimensional turbulence parameterization in mesoscale atmospheric modeling over highly complex terrain. *Journal of Applied Meteorology and Climatology*, *58*(9), 2087–2102. https://doi.org/10.1175/jamc-d-18-0328.1

Haerter, J. O., Berg, P., & Moseley, C. (2017). Precipitation onset as the temporal reference in convective self-organization. *Geophysical Research Letters*, *44*(12), 6450–6459. https://doi.org/10.1002/2017gl073342

Hersbach, H., Bell, B., Berrisford, P., Hirahara, S., Horányi, A., Muñoz-Sabater, J., et al. (2020). The ERA5 global reanalysis. *Quarterly Journal of the Royal Meteorological Society*, *146*(730), 1999–2049. https://doi.org/10.1002/qj.3803

Heus, T., van Heerwaarden, C. C., Jonker, H. J., Siebesma, A. P., Axelsen, S., Dries, K. V. D., et al. (2010). Formulation of the Dutch Atmospheric Large-Eddy Simulation (DALES) and overview of its applications. *Geoscientific Model Development*, *3*(2), 415–444. https://doi.org/10.5194/gmd-3-415-2010

Hong, S.-Y., Noh, Y., & Dudhia, J. (2006). A new vertical diffusion package with an explicit treatment of entrainment processes. *Monthly Weather Review*, *134*(9), 2318–2341. https://doi.org/10.1175/mwr3199.1

Hong, S. Y., & Pan, H. L. (1996). Nonlocal boundary layer vertical diffusion in a medium-range forecast model. *Monthly Weather Review*, *124*(10), 2322–2339. https://doi.org/10.1175/1520-0493(1996)124<2322:nblvdi>2.0.co;2

Honnert, R., Masson, V., & Couvreux, F. (2011). A diagnostic for evaluating the representation of turbulence in atmospheric models at the kilometric scale. *Journal of the Atmospheric Sciences*, *68*(12), 3112–3131. https://doi.org/10.1175/jas-d-11-061.1

Huang, Y., Siems, S. T., Manton, M. J., & Thompson, G. (2014). An evaluation of WRF simulations of clouds over the Southern Ocean with A-Train observations. *Monthly Weather Review*, *142*(2), 647–667. https://doi.org/10.1175/mwr-d-13-00128.1

Iacono, M. J., Delamere, J. S., Mlawer, E. J., Shephard, M. W., Clough, S. A., & Collins, W. D. (2008). Radiative forcing by long-lived greenhouse gases: Calculations with the AER radiative transfer models. *Journal of Geophysical Research*, *113*(D13), D13103. https://doi.org/10.1029/2008jd009944

Ito, J., Niino, H., Nakanishi, M., & Moeng, C.-H. (2015). An extension of the Mellor–Yamada model to the terra incognita zone for dry convective mixed layers in the free convection regime. *Boundary-Layer Meteorology*, *157*(1), 23–43. https://doi.org/10.1007/s10546-015-0045-5

Jiménez, P. A., Dudhia, J., Gonzalez-Rouco, J. F., Navarro, J., Montavez, J. P., & Garcia–Bustamante, E. (2012). A revised scheme for the WRF surface layer formulation. *Monthly Weather Review*, *140*(3), 898–918. https://doi.org/10.1175/mwr-d-11-00056.1

Johnson, K., Giangrande, S., & Toto, T. (2019). Active remote sensing of clouds (ARSCL) product using Ka-band ARM zenith radars (ARSCLKAZRBND1KOLLIAS). *Atmospheric Radiation Measurement (ARM) User Facility*. https://doi.org/10.5439/1393438

Johnson, K., & Jensen, M. (2019). Active remote sensing of Clouds (ARSCL) product using Ka-band ARM zenith radars (ARSCLKAZR1-KOLLIAS). *Atmospheric Radiation Measurement (ARM) User Facility*. https://doi.org/10.5439/1228768

Juliano, T. W., Jiménez, P. A., Kosović, B., Eidhammer, T., Thompson, G., Berg, L. K., et al. (2022). Smoke from 2020 United States wildfires responsible for substantial solar energy forecast errors. *Environmental Research Letters*, *17*(3), 034010. https://doi.org/10.1088/1748-9326/ac5143

Juliano, T. W., Kosović, B., Jiménez, P. A., Eghdami, M., Haupt, S. E., & Martilli, A. (2022). "Gray zone" simulations using a three-dimensional planetary boundary layer parameterization in the Weather Research and Forecasting Model. *Monthly Weather Review*, *150*(7), 1585–1619. https://doi.org/10.1175/mwr-d-21-0164.1

Juliano, T. W., & Lackner, C. P. (2024). Files for "Simulating mixed-phase open cellular clouds observed during COMBLE: Evaluation of parameterized turbulence closure" (Version 4.0) [Dataset]. *Harvard Datavserse*. https://doi.org/10.7910/DVN/U3VI1X

Khanna, S., & Brasseur, J. G. (1998). Three-dimensional buoyancy-and shear-induced local structure of the atmospheric boundary layer. *Journal of the Atmospheric Sciences*, *55*(5), 710–743. https://doi.org/10.1175/1520-0469(1998)055<0710:tdbasi>2.0.co;2

Köhler, M., Ahlgrimm, M., & Beljaars, A. (2013). Unified treatment of dry convective and stratocumulus-topped boundary layers in the ECMWF model. *Quarterly Journal of the Royal Meteorological Society*, *137*, 43–57. https://doi.org/10.1002/qj.713

Koop, T., Luo, B., Tsias, A., & Peter, T. (2000). Water activity as the determinant for homogeneous ice nucleation in aqueous solutions. *Nature*, *406*(6796), 611–614. https://doi.org/10.1038/35020537

Lackner, C. P., Geerts, B., Juliano, T. W., Xue, L., & Kosović, B. (2023). Vertical structure of clouds and precipitation during Arctic cold-air outbreaks and warm-air intrusions: Observations from COMBLE. *Journal of Geophysical Research: Atmospheres*, *128*(13), e2022JD038403. https://doi.org/10.1029/2022jd038403

Lai, H. W., Zhang, F., Clothiaux, E. E., Stauffer, D. R., Gaudet, B. J., Verlinde, J., & Chen, D. (2020). Modeling Arctic boundary layer cloud streets at grey-zone resolutions. *Advances in Atmospheric Sciences*, *37*(1), 42–56. https://doi.org/10.1007/s00376-019-9105-y

Li, D. (2019). Turbulent Prandtl number in the atmospheric boundary layer-where are we now? *Atmospheric Research*, *216*, 86–105. https://doi.org/10.1016/j.atmosres.2018.09.015

Mages, Z., Kollias, P., Zhu, Z., & Luke, E. P. (2023). Surface-based observations of cold-air outbreak clouds during the COMBLE field campaign. *Atmospheric Chemistry and Physics*, *23*(6), 3561–3574. https://doi.org/10.5194/acp-23-3561-2023

Mateling, M. E., Pettersen, C., Kulie, M. S., & L'Ecuyer, T. S. (2023). Marine cold-air outbreak snowfall in the North Atlantic: A CloudSat perspective. *Journal of Geophysical Research: Atmospheres*, *128*(10), e2022JD038053. https://doi.org/10.1029/2022jd038053

Mellor, G. L., & Yamada, T. (1982). Development of a turbulence closure model for geophysical fluid problems. *Reviews of Geophysics*, *20*(4), 851–875. https://doi.org/10.1029/rg020i004p00851

Miller, M. A., Nitschke, K., Ackerman, T. P., Ferrell, W. R., Hickmon, N., & Ivey, M. (2016). The ARM mobile facilities. *The Meteorological Magazine*, *57*(9–1), 9.1–9.15. https://doi.org/10.1175/amsmonographs-d-15-0051.1

Nakanishi, M., & Niino, H. (2009). A development of an improved turbulence closure model for the atmospheric boundary layer. *Journal of the Meteorological Society of Japan. Series II*, *87*(5), 895–912. https://doi.org/10.2151/jmsj.87.895

Neggers, R. A. J., Köhler, M., & Beljaars, A. (2009). A dual mass flux framework for boundary layer convection. Part I: Transport. *Journal of the Atmospheric Sciences*, *66*, 1465–1487. https://doi.org/10.1175/2008JAS2635.1

Niu, G., Yang, Z. L., Mitchell, K. E., Chen, F., Ek, M. B., Barlage, M., et al. (2011). The community Noah land surface model with multi-parameterization options (Noah-MP): 1. Model description and evaluation with local-scale measurements. *Journal of Geophysical Research*, *116*(D12), D12109. https://doi.org/10.1029/2010jd015139

Noh, Y., Cheon, W. G., Hong, S. Y., & Raasch, S. (2003). Improvement of the K-profile model for the planetary boundary layer based on large eddy simulation data. *Boundary-Layer Meteorology*, *107*(2), 401–427. https://doi.org/10.1023/a:1022146015946

Olson, J. B., Kenyon, J. S., Angevine, W., Brown, J. M., Pagowski, M., & Sušelj, K. (2019). *A description of the MYNN-EDMF scheme and the coupling to other components in WRF-ARW*. NOAA Tech. Memo. OAR GSD-61 (37 pp.). https://doi.org/10.25923/n9wm-be49

Oue, M., Tatarevic, A., Kollias, P., Wang, D., Yu, K., & Vogelmann, A. M. (2020). The Cloud-resolving model Radar SIMulator (CR-SIM) Version 3.3: Description and applications of a virtual observatory. *Geoscientific Model Development*, *13*(4), 1975–1998. https://doi.org/10.5194/gmd-13-1975-2020

Papritz, L., & Spengler, T. (2017). A Lagrangian climatology of wintertime cold air outbreaks in the Irminger and Nordic Seas and their role in shaping air–sea heat fluxes. *Journal of Climate*, *8*, 2717–2737. https://doi.org/10.1175/jcli-d-16-0605.1

Pithan, F., Angevine, W., & Mauritsen, T. (2015). Improving a global model from the boundary layer: Total turbulent energy and the neutral limit Prandtl number. *Journal of Advances in Modeling Earth Systems*, *7*(2), 791–805. https://doi.org/10.1002/2014ms000382

Pithan, F., Medeiros, B., & Mauritsen, T. (2014). Mixed-phase clouds cause climate model biases in Arctic wintertime temperature inversions. *Climate Dynamics*, *43*(1–2), 289–303. https://doi.org/10.1007/s00382-013-1964-9

Pithan, F., Svensson, G., Caballero, R., Chechin, D., Cronin, T. W., Ekman, A. M. L., et al. (2018). Role of air-mass transformations in exchange between the Arctic and mid-latitudes. *Nature Geoscience*, *11*, 805–812. https://doi.org/10.1038/s41561-018-0234-1

Rai, R. K., Berg, L. K., Kosović, B., Haupt, S. E., Mirocha, J. D., Ennis, B., & Draxl, C. (2019). Evaluation of the impact of horizontal grid spacing in Terra Incognita on coupled mesoscale-microscale simulations using the WRF framework. *Monthly Weather Review*, *147*(3), 1007–1027. https://doi.org/10.1175/mwr-d-18-0282.1

Renfrew, I. A., & Moore, G. W. K. (1999). An extreme cold-air outbreak over the Labrador Sea: Roll vortices and air–sea interaction. *Monthly Weather Review*, *127*(10), 2379–2394. https://doi.org/10.1175/1520-0493(1999)127<2379:aecaoo>2.0.co;2

Saggiorato, B., Nuijens, L., Siebesma, A. P., de Roode, S., Sandu, I., & Papritz, L. (2020). The influence of convective momentum transport and vertical wind shear on the evolution of a cold air outbreak. *Journal of Advances in Modeling Earth Systems*, *12*(6), e2019MS001991. https://doi.org/10.1029/2019ms001991

Seifert, A., & Heus, T. (2013). Large-eddy simulation of organized precipitating trade wind cumulus clouds. *Atmospheric Chemistry and Physics*, *13*(11), 5631–5645. https://doi.org/10.5194/acp-13-5631-2013

Shin, H. H., & Hong, S. (2015). Representation of the subgrid-scale turbulent transport in convective boundary layers at gray-zone resolutions. *Monthly Weather Review*, *143*(1), 250–271. https://doi.org/10.1175/mwr-d-14-00116.1

Siebesma, A. P., Soares, P. M., & Teixeira, J. (2007). A combined eddy-diffusivity mass-flux approach for the convective boundary layer. *Journal of the Atmospheric Sciences*, *64*(4), 1230–1248. https://doi.org/10.1175/jas3888.1

Simon, J. S., & Chow, F. K. (2021). Alternative anisotropic formulations for eddy-viscosity models in the Weather Research and Forecasting model. *Boundary-Layer Meteorology*, *181*(1), 11–37. https://doi.org/10.1007/s10546-021-00642-0

Skamarock, W. C. (2004). Evaluating mesoscale NWP models using kinetic energy spectra. *Monthly Weather Review*, *132*(12), 3019–3032. https://doi.org/10.1175/mwr2830.1

Skamarock, W. C., & Klemp, J. B. (2008). A time-split nonhydrostatic atmospheric model for weather research and forecasting applications. *Journal of Computational Physics*, *227*(7), 3465–3485. https://doi.org/10.1016/j.jcp.2007.01.037

Skamarock, W. C., Klemp, J. B., Dudhia, J., Gill, D. O., Liu, Z., Berner, J., et al. (2019). *A description of the Advanced Research WRF version 4*. NCAR Technical Note NCAR/TN-556+STR (145 pp.). https://doi.org/10.5065/1dfh-6p97

Smagorinsky, J. (1963). General circulation experiments with the primitive equations: I. The basic experiment. *Monthly Weather Review*, *91*(3), 99–164. https://doi.org/10.1175/1520-0493(1963)091<0099:gcewtp>2.3.co;2

Soares, P. M. M., Miranda, P. M. A., Siebesma, A. P., & Teixeira, J. (2004). An eddy-diffusivity/mass-flux parameterization for dry and shallow cumulus convection. *Quarterly Journal of the Royal Meteorological Society: A Journal of the Atmospheric Sciences, Applied Meteorology and Physical Oceanography*, *130*, 3365–3384. https://doi.org/10.1256/qj.03.223

Stull, R. B. (2012). *An introduction to boundary layer meteorology* (Vol. 13). Springer Science Business Media.

Sušelj, K., Hogan, T. F., & Teixeira, J. (2014). Implementation of a stochastic eddy-diffusivity/mass-flux parameterization into the Navy Global Environmental Model. *Weather and Forecasting*, *29*, 1374–1390. https://doi.org/10.1175/WAF-D-14-00043.1

Thompson, G., & Eidhammer, T. (2014). A study of aerosol impacts on clouds and precipitation development in a large winter cyclone. *Journal of the Atmospheric Sciences*, *71*(10), 3636–3658. https://doi.org/10.1175/jas-d-13-0305.1

Thompson, G., Field, P. R., Rasmussen, R. M., & Hall, W. D. (2008). Explicit forecasts of winter precipitation using an improved bulk microphysics scheme. Part II: Implementation of a new snow parameterization. *Monthly Weather Review*, *136*(12), 5095–5115. https://doi.org/10.1175/2008mwr2387.1

Thompson, G., Rasmussen, R. M., & Manning, K. (2004). Explicit forecasts of winter precipitation using an improved bulk microphysics scheme. Part I: Description and sensitivity analysis. *Monthly Weather Review*, *132*(2), 519–542. https://doi.org/10.1175/1520-0493(2004)132<0519:efowpu>2.0.co;2

Tomassini, L., Field, P. R., Honnert, R., Malardel, S., McTaggart-Cowan, R., Saitou, K., et al. (2017). The "Grey Zone" cold air outbreak global model intercomparison: A cross evaluation using large-eddy simulations. *Journal of Advances in Modeling Earth Systems*, *9*(1), 39–64. https://doi.org/10.1002/2016ms000822

Tornow, F., Ackerman, A. S., & Fridlind, A. M. (2021). Preconditioning of overcast-to-broken cloud transitions by riming in marine cold air outbreaks. *Atmospheric Chemistry and Physics*, *21*(15), 12049–12067. https://doi.org/10.5194/acp-21-12049-2021

Tornow, F., Ackerman, A. S., Fridlind, A. M., Tselioudis, G., Cairns, B., Painemal, D., & Elsaesser, G. (2023). On the impact of a dry intrusion driving cloud-regime transitions in a midlatitude cold-air outbreak. *Journal of the Atmospheric Sciences*, *80*(12), 2881–2896. https://doi.org/10.1175/jas-d-23-0040.1

Torri, G., Kuang, Z., & Tian, Y. (2015). Mechanisms for convection triggering by cold pools. *Geophysical Research Letters*, *42*(6), 1943–1950. https://doi.org/10.1002/2015gl063227

Turner, D. D., Clough, S. A., Liljegren, J. C., Clothiaux, E. E., Cady-Pereira, K. E., & Gaustad, K. L. (2007). Retrieving liquid water path and precipitable water vapor from the atmospheric radiation measurement (ARM) microwave radiometers. *IEEE Transactions on Geoscience and Remote Sensing*, *45*(11), 3680–3689. https://doi.org/10.1109/TGRS.2007.903703

Witek, M. L., Teixeira, J., & Matheou, G. (2011). An integrated TKE-based eddy diffusivity/mass flux boundary layer closure for the dry convective boundary layer. *Journal of the Atmospheric Sciences*, *68*, 1526–1540. https://doi.org/10.1175/2011JAS3548.1

Wu, P., & Ovchinnikov, M. (2022). Cloud morphology evolution in Arctic cold-air outbreak: Two cases during COMBLE period. *Journal of Geophysical Research: Atmospheres*, *127*(10), e2021JD035966. https://doi.org/10.1029/2021jd035966

Wyngaard, J. C. (2004). Toward numerical modeling in the "Terra Incognita". *Journal of the Atmospheric Sciences*, *61*(14), 1816–1826. https://doi.org/10.1175/1520-0469(2004)061<1816:tnmitt>2.0.co;2

Yang, Z.-L., Niu, G. Y., Mitchell, K. E., Chen, F., Ek, M. B., Barlage, M., et al. (2011). The community Noah land surface model with multi-parameterization options (Noah-MP): 2. Evaluation over global river basins. *Journal of Geophysical Research*, *116*. https://doi.org/10.1029/2010JD015140

Young, G. S., Kristovich, D. A., Hjelmfelt, M. R., & Foster, R. C. (2002). Rolls, streets, waves, and more: A review of quasi-two-dimensional structures in the atmospheric boundary layer. *Bulletin America Meteorology Social*, *83*(7), 997–1002. https://doi.org/10.1175/1520-0477(2002)083<0997:rswama>2.3.co;2

Zhang, D. (2019). *MWR retrievals (MWRRET1LILJCLOU)*. Atmospheric Radiation 755 Measurement (ARM) User Facility. https://doi.org/10.5439/1027369

Zhang, X., Bao, J., Chen, B., & Grell, E. D. (2018). A three-dimensional scale-adaptive turbulent kinetic energy scheme in the WRF-ARW model. *Monthly Weather Review*, *146*(7), 2023–2045. https://doi.org/10.1175/mwr-d-17-0356.1

Zhou, B., Simon, J. S., & Chow, F. K. (2014). The convective boundary layer in the Terra Incognita. *Monthly Weather Review*, *146*(7), 2545–2563. https://doi.org/10.1175/jas-d-13-0356.1

Zonato, A., Martilli, A., Jiménez, P. A., Dudhia, J., Zardi, D., & Giovannini, L. (2022). A new K-ϵ turbulence parameterization for mesoscale meteorological models. *Monthly Weather Review*, *150*(8), 2157–2174. https://doi.org/10.1175/mwr-d-21-0299.1